



Extinction of incident hydrogen/air detonation in fine water sprays

Cite as: Phys. Fluids **33**, 116109 (2021); <https://doi.org/10.1063/5.0071405>

Submitted: 14 September 2021 • Accepted: 17 October 2021 • Published Online: 19 November 2021

 Yong Xu (徐勇), Majie Zhao (赵马杰) and  Huangwei Zhang (张黄伟)



View Online



Export Citation



CrossMark

Physics of Fluids

SPECIAL TOPIC: Flow and Acoustics of Unmanned Vehicles

Submit Today!



Extinction of incident hydrogen/air detonation in fine water sprays

Cite as: Phys. Fluids **33**, 116109 (2021); doi: [10.1063/5.0071405](https://doi.org/10.1063/5.0071405)

Submitted: 14 September 2021 · Accepted: 17 October 2021 ·

Published Online: 19 November 2021



View Online



Export Citation



CrossMark

Yong Xu (徐勇), Majie Zhao (赵马杰), and Huangwei Zhang (张黄伟) ^{a)}

AFFILIATIONS

Department of Mechanical Engineering, National University of Singapore, 9 Engineering Drive 1, Singapore 117576, Republic of Singapore

^{a)} Author to whom correspondence should be addressed: huangwei.zhang@nus.edu.sg. Tel.: +65 6516 2557. Fax: +65 6779 1459

ABSTRACT

Two-dimensional numerical simulations with Eulerian–Lagrangian method are conducted to study propagation and extinction of stoichiometric hydrogen/air detonations in fine water sprays. Parameterized by water mass loading and droplet size, a detonation extinction map is predicted. Detonation extinction occurs with larger mass loading and/or smaller droplet size. General features of water droplets and local detonation frontal structures are well captured. Numerical soot foils are used to characterize the influence of mass loading and droplet size on the detonation wave. The results also show that the detonation cell size increases with increased mass loading or decreased droplet size. Analysis on unsteady detonation extinction process is performed with the evolutions of detonation frontal structure, spatial distribution of thermochemical variables, and interphase transfer rates (mass, energy, and momentum). Moreover, the chemical explosive mode analysis reveals that for stable detonation, thermal runaway dominates behind the Mach stem, while chemical propensities of autoignition and thermal runaway appear alternately behind the incident wave. When the induction zone length increases as the reaction front (RF) and shock front (SF) are decoupled, localized burned pockets surrounded by the autoignition chemical explosive mixture can be observed. In addition, the interactions between detonation wave and water droplets demonstrate that the energy and momentum transfer have more direct interaction with SF and RF than the mass transfer. The interphase transfer rates increase with the water mass loading. Under the same mass loading, the smaller the droplet size, the larger the interphase transfer rates. However, the size of fine water droplets has a limited influence on the interphase momentum exchange. Moreover, high energy and mass transfer rates are observed at the onset of detonation extinction, and they gradually decrease when the reaction and detonation fronts are decoupled.

Published under an exclusive license by AIP Publishing. <https://doi.org/10.1063/5.0071405>

NOMENCLATURE

A_d	Surface area of a single droplet (m^2)
$\mathbf{a}_e, \mathbf{b}_e$	The right and left eigenvectors associated with the CEM
a_i, b_i	Constant related to $c_{p,d}$
C_d	Drag coefficient
C_p	Heat capacity at constant pressure (J/kg K)
$C_{p,m}$	Heat capacity of m th species at constant pressure (J/kg K)
C_v	Heat capacity at constant volume (J/kg K)
c_g	Vapor concentration in the surrounding gas (kmol/m^3)
$c_{p,d}$	Droplet heat capacity at constant pressure (J/kg K)
c_s	Vapor mass concentration (kmol/m^3)
\mathbf{D}	Deformation gradient tensor
D_f	Vapor mass diffusivity in the gas phase (m^2/s)
D_m	Mass diffusivity (m^2/s)

d_d	Droplet material diameter (m)
d_d^0	Initial water droplet diameter (m)
E	Total non-chemical energy (J/kg)
e	Specific sensible internal energy (J/kg)
\mathbf{F}_d	Drag force on the droplet (N)
h_c	Convective heat transfer coefficient ($\text{W/m}^2 \text{K}$)
h_g	Enthalpy of water vapor (J/kg)
$h(T_d)$	Heat of vaporization at the droplet temperature (J/kg)
\mathbf{I}	Unit tensor
\mathbf{J}_ω	Jacobian matrix of the chemical source
\mathbf{j}	Diffusive heat flux (W/m^2)
k	Thermal conductivity coefficient (W/m K)
k_c	Mass transfer coefficient (m/s)
L_{ind}	Induction zone length (m)
Le_m	Lewis number of m th species

M	Total species number
m_d	Mass of a single droplet (kg)
\dot{m}_d	Evaporation rate (kg/s)
\dot{m}_f	Vapor mass flux (kg/m ² s)
N_d	Droplet number in one cell
Nu	Nusselt number
n_p	Droplet number per parcel
p	Pressure (Pa)
Pr	Prandtl number
p_{Sat}	Saturation pressure of droplet (Pa)
\dot{Q}_c	Convective heat transfer rate (J/s)
\dot{Q}_{lat}	Latent heat transfer rate (J/s)
R	Specific gas constant (J/kg K)
R_u	Universal gas constant (J/mol K)
Re_d	Droplet Reynolds number
Sc	Schmidt number
Sh	Sherwood number
s_m	Species mass flux (kg/m ² s)
S_{mass}	Mass transfer rate (kg/m ³ s)
S_{mom}	Momentum transfer rate (N/m ³)
S_{energy}	Energy transfer rate (J/m ³ s)
$S_{species,m}$	Species transfer rate (kg/m ³ s)
T	Gas temperature (K)
\mathbf{T}	Viscous stress tensor (kg/m s ²)
T_c	Critical temperature (K)
T_d	Droplet temperature (K)
T_f	Droplet surface temperature (K)
t	Time (s)
\mathbf{u}	Velocity vector (m/s)
\mathbf{u}_d	Droplet velocity vector (m/s)
V_c	CFD cell volume (m ³)
V_1, V_2	Constant related to vapor mass diffusivity
W_d	Molar weight of the vapor (kg/mol)
W_m	Molar weight of m th species (kg/mol)
x_i	Fuel vapor mole fraction in the surrounding gas
x_{TR}	Transition loci for thermal runaway and radical explosion (m)
Y_m	Mass fraction of m th species
\mathbf{y}	Vector of temperature or species mass fractions (K)
z	Mass loading

Greek letters

α	Thermal diffusivity coefficient (m ² /s)
$\Delta h_{f,m}^0$	Formation enthalpy of m th species (J/mol)
λ_e	Eigenvalues of the <i>Jacobian</i> matrix associated with the eigenvalues of \mathbf{J}_ω (1/s)
μ	Dynamic viscosity (kg/m s)
ρ	Gas density (kg/m ³)
ρ_d	Droplet material density (kg/m ³)
τ	Timescale (s)
τ_{chem}	Chemical timescale (s)
$\omega(\mathbf{y})$	Chemical source term (K/s or 1/s)
$\dot{\omega}_m$	Production or consumption rate of m th species (kg/m ³ s)
$\dot{\omega}_T$	Heat release from chemical reactions (J/m ³ s)
ϱ	Water apparent density (kg/m ³)

Superscripts

\mathbf{T}	Transpose
0	Initial value

Subscripts

c	Critical, coefficient, convective, CFD cell
$chem$	Chemical reaction
d	Droplet, drag, water vapor
e	Eigenvalue
$energy$	Energy
f	Gas phase, droplet surface
g	Surrounding gas, water vapor
i	i th condensed species vapor
ind	Induction
lat	Latent
m	Mass, m th species
$mass$	Mass
mom	Momentum
p	Parcel
s	Surface
sat	Saturation
$species$	Species
TR	Transition
u	Universal
v	Volume
ω	Chemical source term
$1, 2$	Diffusion species

Acronym

AI	Autoignition
CEM	Chemical explosive mode
CEMA	Chemical explosive mode analysis
DW	Detonation wave
EI	Explosion index
EOF	Evaporation onset front
ETS	End of two-phase section
HRL	Half-reaction length (m)
HRR	Heat release rate (J/m ³ s)
IW	Incident wave
JF1	Primary jet flow
JF2	Secondary jet flow
MS	Mach stem
RF	Reaction front
RMI	Richtmyer–Meshkov instability
SF	Shock front
SP	Sonic plane
TP1	Primary triple point
TP2	Secondary triple point
TW	Transverse wave
ZND	Zel'dovich, Neumann, and Döring

I. INTRODUCTION

There is increased interest in exploring effective approaches to mitigate detonation of flammable gas, related to prevention from

explosion hazards and industrial safety assessment.^{1,2} Water is an ideal detonation mitigant due to numerous advantages.^{3,4} Specifically, it can absorb considerable heat from gas phase due to large heat capacity and latent heat of evaporation.⁵ Also, it is readily available with low cost and lots of flexibilities. Meanwhile, use of water would not bring environmental pollution. Moreover, as a solution, it is possible to include proper additives, for example, alkali salts (KCl and NaCl),⁶ for better explosion inhibition. There are various forms of water utilized for detonation or explosion mitigation,^{5,7,8} for example, solid jet, diffused jet, and water mists. The last one is most promising since sprayed water droplets have large specific surface area and low terminal velocity, which allow them to continuously circulate in the explosion area in a manner of a total flooding gas. It therefore can effectively weaken the blast, inhibit chemical reaction, and reduce gas temperature. Although it has been widely used in various areas, for example, process and energy industries, nuclear power plants, and even space applications, however, the mechanisms behind detonation/explosion inhibition with water mists are still not well understood.

There have been a series of studies about propagation of shock/blast waves in water sprays. For instance, Jourdan *et al.*⁹ use water aerosol shock tube experiments to study shock attenuation in a cloud of water droplets. They characterize shock attenuation with shock tube (i.e., cross-sectional area) and droplet properties (e.g., total water volume, droplet size, loading rate, and droplet specific surface area). With the similar experimental conditions, Chauvin *et al.*¹⁰ find the peculiar pressure evolution after the transmitted shock wave in two-phase mixture and they also measure the overpressures under different water spray conditions. Moreover, Adiga *et al.*¹¹ unveil the physical picture of fine water droplet breakup in detonation process and quantify the droplet fragmentation with breakup energy. Eulerian–Lagrangian simulations by Ananth *et al.*¹² are performed to examine the effects of mono-dispersed fine water mist on a confined blast. It is found that the latent heat absorption is dominant for blast mitigation, followed by convective heat transfer and momentum exchange. Furthermore, Schwer and Kailasanath¹³ simulate unconfined explosions in water sprays, and find that the water mists can dampen the shock through vaporization and momentum extraction. Different from the observations by Ananth *et al.*,¹² they claim that the momentum extraction plays a more important role in weakening the blast.

In the above-mentioned studies, the effects of water mists on chemical reactions are not discussed, since they use air as the carrier gas (e.g., Refs. 9 and 10) specify the chemically equilibrium gas from an explosion (e.g., Ref. 12) or there is no direct interaction between water droplets and post-shock reaction zone (e.g., Ref. 13). It is well known that detonation is a complex of coupled shock and reaction fronts, and therefore, additional complexities may arise in droplet–detonation interactions. Thomas *et al.*¹⁴ experimentally study detonations of hydrogen, ethane, and acetylene with water sprays in a vertical tube. They attribute detonation failure to high heat loss due to water droplets compared to the combustion heat release. They also find that the water droplet size and loading densities are crucial to quenching a detonation. It is observed by Niedzielska *et al.*¹⁵ that small (215 μm in their experiments) droplets with fast evaporation rate have strong influence on detonation quenching. Moreover, from detonation tube experiments, Jarsalé *et al.*¹⁶ observe that the presence of water spray drastically alters the detonation cell size, but the ratio of the hydrodynamic thickness to the cell size remains constant, regardless of

water droplet addition. The effects of water mists on deflagration-to-detonation transition (DDT) are also demonstrated with reduced overpressure and delayed timing of detonation development.⁸

In addition to the foregoing experimental work,^{8,14–16} recent computational efforts provide us more insights on detonation in water sprays. For example, Song and Zhang simulate the methane detonation and find that the inhibition effects of water sprays are mainly reflected in reduction of flame temperature.⁷ Watanabe *et al.* observe that the dispersed water droplets significantly alter the detonation flow field, and water droplet evaporation mainly occurs around 10 mm behind the leading shock.¹⁷ Furthermore, the cellular patterns of dilute water spray detonation are more regular than those of the droplet-free detonations.¹⁸ The interactions between detonation wave and water droplets change the hydrodynamic thickness. Exchange of mass, momentum, and energy between two phases occurs within the hydrodynamic thickness, which lowers the detonation velocity and fluctuations downstream of the leading shock front. Their results also show that droplet breakup mainly occurs near the shock front,¹⁹ and the average diameter of the disintegrated water droplets is independent of the initial propagation velocity of the shock front. However, in these numerical studies, detonation extinction due to water sprays is not investigated.

The droplet size and mass loading considered in the above studies are summarized in Fig. 1. One can see that most of the droplet diameters are above 20 μm , corresponding to the mass loading of 0.03–13.3. It is well known that fine or ultra-fine water droplets with diameter less than 20 μm have outstanding performance in fire suppression, due to fast evaporation rate and high specific surface area.^{3,4} Nevertheless, their effectiveness and the critical spray properties for detonation extinction and how the sprayed droplets interact with the detonation have not been reported yet. In this work, propagation and

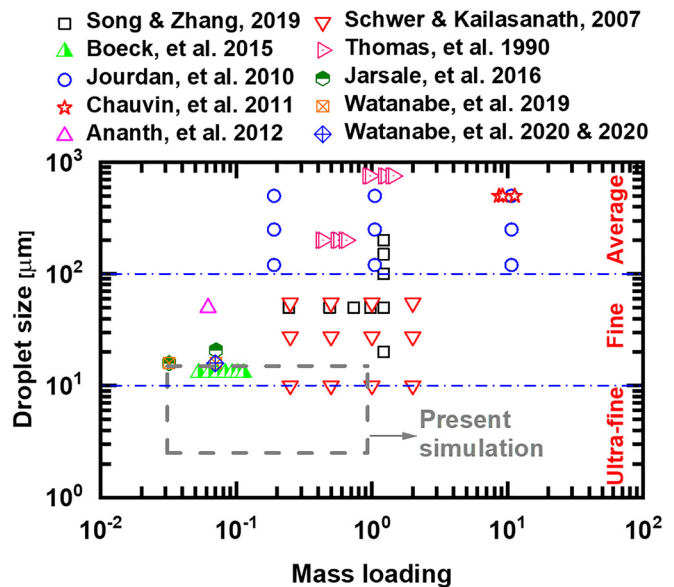


FIG. 1. Studies of detonation and shock in water sprays. Droplet diameter spectrum (dashed-dotted lines) follows Grant *et al.*⁵ Average: droplet diameter range most relevant for firefighting.

extinction of incident hydrogen/air detonation in fine or ultra-fine water droplets will be computationally studied. As marked in Fig. 1, the droplet diameters considered in the present simulations range from 2.5 to 15 μm , while the mass loading is 0.031–0.93. The Eulerian–Lagrangian approach with two-way gas–liquid coupling is used to model the compressible, multispecies, and two-phase reacting flows. The chemical explosive mode analysis (CEMA)^{20,21} is applied to extract the detailed information about the chemical reaction in gaseous detonations. Emphasis is laid on the interactions between gas phase and droplet phase, as well as the chemical structure evolutions when the hydrogen/air detonation extinction process. The rest of this paper is structured as below. The governing equation and numerical implementations will be presented in Sec. II, while the physical model will be detailed in Sec. III. The results will be presented in Sec. IV, followed by the discussion in Sec. V. The main findings are summarized in Sec. VI.

II. GOVERNING EQUATIONS AND COMPUTATIONAL METHOD

A. Gas phase

The governing equations of mass, momentum, energy, and species mass fraction are solved with the ideal gas equation of state. They, respectively, read

$$\frac{\partial \rho}{\partial t} + \nabla \cdot [\rho \mathbf{u}] = S_{mass}, \quad (1)$$

$$\frac{\partial(\rho \mathbf{u})}{\partial t} + \nabla \cdot [\mathbf{u}(\rho \mathbf{u})] + \nabla p + \nabla \cdot \mathbf{T} = \mathbf{S}_{mom}, \quad (2)$$

$$\frac{\partial(\rho \mathbf{E})}{\partial t} + \nabla \cdot [\mathbf{u}(\rho \mathbf{E} + \mathbf{p})] + \nabla \cdot [\mathbf{T} \cdot \mathbf{u}] + \nabla \cdot \mathbf{j} = \dot{\omega}_T + S_{energy}, \quad (3)$$

$$\frac{\partial(\rho Y_m)}{\partial t} + \nabla \cdot [\mathbf{u}(\rho Y_m)] + \nabla \cdot \mathbf{s}_m = \dot{\omega}_m + S_{species,m} \quad (m = 1, \dots, M-1), \quad (4)$$

$$p = \rho RT. \quad (5)$$

In above equations, t is time and $\nabla \cdot (\cdot)$ is the divergence operator. ρ is the gas density, \mathbf{u} is the velocity vector, T is the gas temperature, and p is the pressure, which is updated from the equation of state, that is, Eq. (5). Y_m is the mass fraction of m th species, and M is the total species number. Only $(M-1)$ equations are solved in Eq. (4) and the mass fraction of the inert species (e.g., nitrogen) is recovered from $\sum_{m=1}^M Y_m = 1$. $\mathbf{E} \equiv e + |\mathbf{u}|^2/2$ is the total non-chemical energy, and e is the sensible internal energy. R in Eq. (5) is the specific gas constant and is calculated from $R = R_u \sum_{m=1}^M Y_m W_m^{-1}$. W_m is the molar weight of m th species and $R_u = 8.314 \text{ J}/(\text{mol} \cdot \text{K})$ is the universal gas constant. The source terms in Eqs. (1)–(4), that is, S_{mass} , \mathbf{S}_{mom} , S_{energy} , and $S_{species,m}$, denote the exchanges of mass, momentum, energy, and species between gas and liquid phases. Their corresponding expressions are given in Eqs. (26)–(29), respectively.

The viscous stress tensor \mathbf{T} in Eq. (2) is modeled by

$$\mathbf{T} = -2\mu \text{dev}(\mathbf{D}). \quad (6)$$

Here, μ is the dynamic viscosity and follows the Sutherland's law.²² Moreover, $\text{dev}(\mathbf{D}) = \mathbf{D} - \text{tr}(\mathbf{D})\mathbf{I}/3$ is the deviatoric component of the deformation gradient tensor $\mathbf{D} \equiv [\nabla \mathbf{u} + (\nabla \mathbf{u})^T]/2$. \mathbf{I} denotes the unit tensor.

In addition, \mathbf{j} in Eq. (3) is the diffusive heat flux and can be modeled with Fourier's law, that is,

$$\mathbf{j} = -k \nabla T. \quad (7)$$

Thermal conductivity k is calculated using the Eucken approximation,²³ that is, $k = \mu C_v(1.32 + 1.37R/C_v)$, where C_v is the heat capacity at constant volume and derived from $C_v = C_p - R$. Here, $C_p = \sum_{m=1}^M Y_m C_{p,m}$ is the heat capacity at constant pressure, and $C_{p,m}$ is estimated from JANAF polynomials.²⁴

In Eq. (4), $\mathbf{s}_m = -D_m \nabla(\rho Y_m)$ is the species mass flux. $D_m = \alpha/Le_m$ is the mass diffusivity. The unity Lewis number assumption ($Le_m = 1$) is used, which is reasonable because detonation is dominated by shock-compression ignition. Therefore, D_m can be calculated through $D_m = k/\rho C_p$. Moreover, $\dot{\omega}_m$ is the production or consumption rate of m th species by all N reactions

$$\dot{\omega}_m = W_m \sum_{j=1}^N \omega_{m,j}^o. \quad (8)$$

$\omega_{m,j}^o$ is the reaction rate of each elementary reaction. Also, the term $\dot{\omega}_T$ in Eq. (3) represents the heat release from chemical reactions and is estimated as $\dot{\omega}_T = -\sum_{m=1}^M \dot{\omega}_m \Delta h_{f,m}^o$. $\Delta h_{f,m}^o$ is the formation enthalpy of m th species.

In this study, the effects of water droplet volume fraction are not included in Eqs. (1)–(5), since dilute water sprays are considered. However, droplet preferential accumulation may occur, for example, behind the shock wave, leading to localized high droplet volume fractions.^{17–19} Comparative analysis with and without droplet volume fraction in the formulations is thereby performed in Sec. A of the supplementary material, and it is found that Eqs. (1)–(5) can well capture detonation extinction dynamics in the studied problems.

B. Liquid phase

The Lagrangian method is used to model the dispersed liquid phase, which is composed of a large number of spherical droplets.²⁵ Collision between the droplets is neglected because we only study the dilute water sprays with the initial droplet volume fraction being generally less than 0.1%.²⁶ Also, droplet breakup is not considered in this work. Therefore, the equations of mass, momentum, and energy for a single droplet are

$$\frac{dm_d}{dt} = -\dot{m}_d, \quad (9)$$

$$\frac{d\mathbf{u}_d}{dt} = \frac{\mathbf{F}_d}{m_d}, \quad (10)$$

$$c_{p,d} \frac{dT_d}{dt} = \frac{\dot{Q}_c + \dot{Q}_{lat}}{m_d}, \quad (11)$$

where $m_d = \pi \rho_d d_d^3/6$ is the mass of a single droplet, and ρ_d and d_d are the droplet material density and diameter, respectively. \mathbf{u}_d is the droplet velocity vector, and \mathbf{F}_d is the force exerted on the droplet. $c_{p,d}$ is the droplet heat capacity at constant pressure, and T_d is the droplet temperature. In this work, both ρ_d and $c_{p,d}$ are dependent on the droplet temperature T_d ,²⁷ that is,

$$\rho_d(T_d) = \frac{a_1}{a_2^{1+(1-T_d/a_3)^{a_4}}}, \quad (12)$$

$$c_{p,d}(T_d) = \frac{b_1^2}{\tau} + b_2 - \tau \left\{ 2.0b_1b_3 + \tau \left\{ b_1b_4 + \tau \left[\frac{1}{3}b_3^2 + \tau \left(\frac{1}{2}b_3b_4 + \frac{1}{5}\tau b_4^2 \right) \right] \right\} \right\}, \quad (13)$$

where a_i and b_i are constants and can be found from Ref. 27. In Eq. (13), $\tau = 1.0 - \min(T_d, T_c)/T_c$, where T_c is the critical temperature.

The evaporation rate, \dot{m}_d , in Eq. (9) is modeled through

$$\dot{m}_d = \dot{m}_f A_d, \quad (14)$$

where A_d is the surface area of a single droplet. The vapor mass flux from the droplet into the gas phase, \dot{m}_f , is calculated as^{28,29}

$$\dot{m}_f = k_c W_d (c_s - c_g). \quad (15)$$

Its accuracy has been confirmed through validations against the experimental data of single droplet evaporation.³⁰ W_d is the molecular weight of the vapor. c_s is the vapor mass concentration at the droplet surface, that is,

$$c_s = \frac{p_{sat}}{R_u T_f}, \quad (16)$$

where p_{sat} is the saturation pressure and is obtained under the assumption that the vapor pressure at the droplet surface is equal to that of the gas phase. The droplet surface temperature is calculated from $T_f = (T + 2T_d)/3$.²⁹ In Eq. (15), the vapor concentration in the surrounding gas, c_g , is obtained from

$$c_g = \frac{p x_i}{R_u T_f}, \quad (17)$$

where x_i is the vapor mole fraction in the surrounding gas. The mass transfer coefficient, k_c , in Eq. (15) is calculated from the Sherwood number Sh ,³¹ that is,

$$Sh_{ab} = \frac{k_c d_d}{D_f} = 2.0 + 0.6 Re_d^{1/2} Sc^{1/3}, \quad (18)$$

where Sc is the Schmidt number of gas phase. The droplet Reynolds number in Eq. (18), Re_d , is defined based on the interphase velocity difference

$$Re_d \equiv \frac{\rho d_d |\mathbf{u}_d - \mathbf{u}|}{\mu}. \quad (19)$$

Moreover, D_f in Eq. (18) is the vapor mass diffusivity in the gas phase³²

$$D_f = 10^{-3} \frac{T_s^{1.75}}{p_s} \sqrt{\frac{1}{W_d} + \frac{1}{W_m}} / \left(V_1^{1/3} + V_2^{1/3} \right)^2, \quad (20)$$

where V_1 and V_2 are constants.³³

Since the ratio of gas density to the water droplet material density is well below one, the Basset force, history force, and gravity force are not considered.²⁶ Only the Stokes drag \mathbf{F}_d is considered in Eq. (10) and modeled as (assuming that the droplet is spherical)³⁴

$$\mathbf{F}_d = \frac{18\mu C_d Re_d}{\rho_d d_d^2} m_d (\mathbf{u} - \mathbf{u}_d). \quad (21)$$

The drag coefficient in Eq. (21), C_d , is estimated as³⁴

$$C_d = \begin{cases} 0.424 & \text{if } Re_d \geq 1000, \\ \frac{24}{Re_d} \left(1 + \frac{1}{6} Re_d^{2/3} \right) & \text{if } Re_d < 1000. \end{cases} \quad (22)$$

It has been shown by Cheatham and Kailasanath³⁵ that Eq. (22) can correctly predict the velocity distributions of a flow field with shock waves, and has the comparable accuracies to other models for drag coefficients.^{36–38} It is also shown that the predictions are not sensitive to these sub-models. Pressure gradient force is neglected, since it is generally two orders of magnitude smaller than the drag force, based on a *posterior* analysis of our simulation results (see Sec. B in the [supplementary material](#)).

The convective heat transfer rate \dot{Q}_c in Eq. (11) is calculated from

$$\dot{Q}_c = h_c A_d (T - T_d). \quad (23)$$

Here, h_c is the convective heat transfer coefficient and computed using the correlation by Ranz and Marshall,³¹ that is,

$$Nu = h_c \frac{d_d}{k} = 2.0 + 0.6 Re_d^{1/2} Pr^{1/3}, \quad (24)$$

where Nu and Pr are the Nusselt and Prandtl numbers of gas phase, respectively. In addition, the heat transfer associated with droplet evaporation, \dot{Q}_{lat} in Eq. (11), is

$$\dot{Q}_{lat} = -\dot{m}_d h(T_d), \quad (25)$$

where $h(T_d)$ is the heat of vaporization at the droplet temperature T_d .

Two-way coupling between the gas and liquid phases is enforced in this work. The corresponding terms, S_{mass} , S_{mom} , S_{energy} , and $S_{species,m}$ in Eqs. (1)–(4), are calculated based on the contributions from each droplet in the CFD cells, which read

$$S_{mass} = \frac{1}{V_c} \sum_1^{N_d} \dot{m}_d, \quad (26)$$

$$S_{mom} = -\frac{1}{V_c} \sum_1^{N_d} (-\dot{m}_d \mathbf{u}_d + \mathbf{F}_d), \quad (27)$$

$$S_{energy} = -\frac{1}{V_c} \sum_1^{N_d} (-\dot{m}_d h_g + \dot{Q}_c), \quad (28)$$

$$S_{species,m} = \begin{cases} S_{mass} & \text{for } H_2O \text{ species,} \\ 0 & \text{for other species.} \end{cases} \quad (29)$$

In the following, S_{mass} , S_{mom} , and S_{energy} are termed as mass, momentum, and energy transfer rates, respectively. Here, V_c is the CFD cell volume and N_d is the droplet number in one cell. $-\dot{m}_d \mathbf{u}_d$ is the momentum transfer due to droplet evaporation, whereas $-\dot{m}_d h_g$ is the energy transfer by water vapor addition (h_g is enthalpy of water vapor at droplet temperature).

C. Computational method

The gas and liquid phase governing equations are solved by a compressible two-phase reacting flow solver, *RYrhoCentralFoam*,³⁹ which is customized from the fully compressible non-reacting flow solver *rhoCentralFoam* in OpenFOAM 6.0.⁴⁰ *rhoCentralFoam* is extensively validated using the Sod's problem, forward step, supersonic jet, and shock–vortex interaction.^{41,42} Moreover, *RYrhoCentralFoam*

has been extensively validated and verified for detonation problems in gaseous and gas–droplet two-phase flows, and good agreements are achieved about detonation frontal structure, cell size, propagation speed, and gas–liquid two-phase coupling.³⁹ It has been successfully applied for various detonation problems.^{43–47}

Second-order implicit backward method is employed for temporal discretization, and the time step is about 1×10^{-11} s (maximum Courant number < 0.1). The KNP (i.e., Kurganov *et al.*⁴⁸) scheme with van Leer limiter is used for MUSCL-type reconstructions of the convective fluxes in momentum equation. Total Variation Diminishing (TVD) scheme is used for the convective terms in energy and species mass fraction equations. Also, second-order central differencing scheme is applied for the diffusion terms in Eqs. (2)–(4). The hydrogen mechanism with 9 species and 19 reactions⁴⁹ is used, which is validated against the measured ignition delay and detonation cell size.³⁹

For the liquid phase, the droplets are tracked based on their barycentric coordinates. The equations, that is, Eqs. (9)–(11), are solved by first-order implicit Euler method. Meanwhile, the gas properties at the droplet location [e.g., the gas velocity in Eq. (19) and temperature in Eq. (22)] are calculated based on linear interpolation. More detailed information about the numerical methods for gas and liquid phases can be found in Ref. 39.

III. PHYSICAL MODEL

The computational domain is shown in Fig. 2. The length (x -direction) and width (y -direction) are 0.3 and 0.025 m, respectively. It includes driver, development, and two-phase sections, as marked in Fig. 2. They are initially filled with stoichiometric H_2 /air premixture, with temperature and pressure being $T_0 = 300$ K and $p_0 = 50$ kPa, respectively. Uniform Cartesian cells are used to discretize the domain, and the mesh cell size transitions from 160 μ m in the driver section, 80 μ m in the development section, to 20 μ m in the two-phase section. The total cell numbers in the three sections are 102 400, 409 600, and 6 250 000, respectively. The half-reaction length (HRL) estimated from the purely gaseous Zel'dovich, Neumann, and Döring (ZND) structure of H_2 /air detonation is 309 μ m. Therefore, the resolution in the two-phase section, where our analysis is focused, is approximately 15 cells per HRL. In the two-phase section, the induction zone is thickened due to heat absorption and momentum extraction by droplets. Therefore, in spray detonation, the number of cells in induction zone may be larger than 15. The total length of the driver and development sections is about 647 HRL and hence sufficient to minimize the detonation initiation effects before the detonation wave (DW) is transmitted into the two-phase section.⁵⁰ Mesh sensitivity analysis is provided

in Sec. C of the [supplementary material](#), and the results confirm the sufficiency of the above resolution for the gas phase.

The DW is initiated by three vertically placed hot spots (2000 K and 50 atm) at the left end (see Fig. 2), and the interactions between the shock waves can quickly lead to the detonation frontal instability. The pure gas result when the DW lies at $x = 0.2$ m (slightly before the two-phase section) is used as the initial field for all the two-phase simulations. The upper and lower boundaries of the domain in Fig. 2 are assumed to be periodic. For the left boundary ($x = 0$), the non-reflective condition is enforced for the pressure, while the zero gradient condition for other quantities.⁵¹ Since the gas before the detonation wave is static, the boundary condition at $x = 0.3$ m is not relevant and in our simulations zero gradient conditions are assumed.⁵²

The monodispersed spherical water droplets are uniformly distributed in the two-phase section (i.e., $x = 0.22$ – 0.3 m). The initial water droplet diameters d_d^0 range from 2.5 to 15 μ m, which roughly correspond to the dominant sizes of the water droplets from ultrasonic mist generators.⁵³ Although water droplet polydispersity is ubiquitous in practical scenarios,^{14,16} however, monodispersed droplets are helpful for pinpointing the droplet size effects. The polydispersity effects are not considered in this work and merit a separate study. The resultant ratios of Eulerian mesh size to droplet diameter range from 1.3 to 8. As such, for larger droplets, for example, 15 μ m, the evaporation rate may be under-predicted, based on the single droplet calculations in Sec. E of the [supplementary material](#). The mass loading $z = 0.031$ – 0.93 will be studied in this work, corresponding to water apparent density ρ of 0.013– 0.391 kg/m³. Note that z (or ρ) is estimated as the ratio of the total water mass to the mass (or volume) of the gaseous mixture within the droplet-containing region.²⁶ The initial temperature, material density, and isobaric heat capacity of the water droplets are 300 K, 997 kg/m³, and 4187 J/kg K, respectively. In addition, the water droplets are assumed to be initially stationary (i.e., $\mathbf{u}_d = 0$), which is reasonable due to typically small terminal velocities of fine water droplets.^{9,10} Computational parcel is used in the simulations, and water droplet number in each parcel is assumed to be $n_p = 10$. This resolution is sufficient for capturing droplet evolutions and interphase coupling (see Sec. F of the [supplementary material](#)).

IV. RESULTS

A. Detonation extinction diagram

A series of H_2 /air detonations in water mists is simulated in this work. They are parameterized by a range of initial droplet diameter d_d^0 and mass loading z (or apparent density ρ), which are summarized in Fig. 3. The water vapor mass fraction in the mixture (Y_{H_2O}) is also

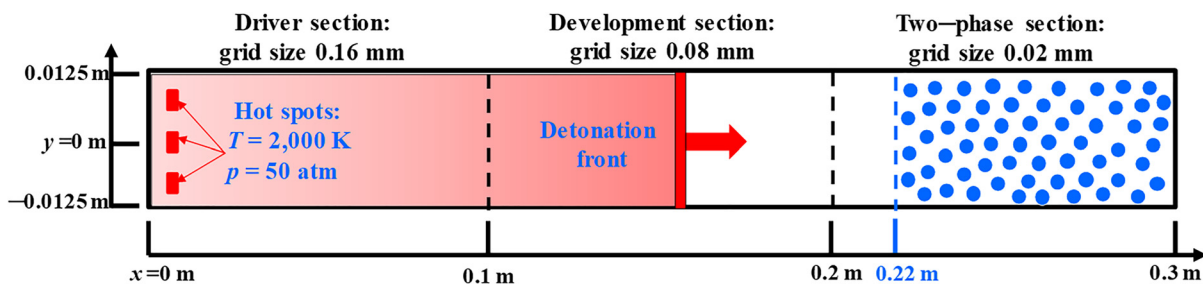


FIG. 2. Schematic of the computational domain. Blue dots: water droplets.

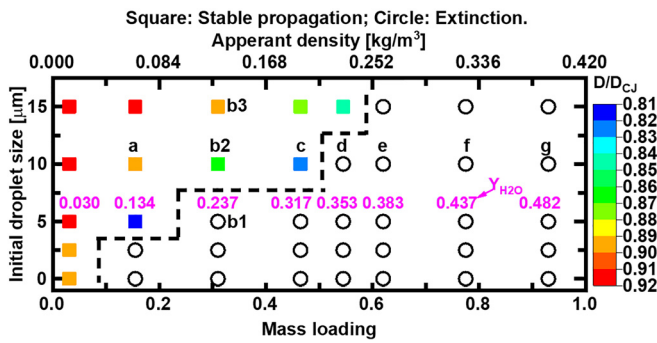


FIG. 3. Diagram of two-phase detonation propagation and extinction. Y_{H_2O} : water vapor mass fraction when all the droplets are vaporized. The cases with $0 \mu\text{m}$ have fully vaporized water with the corresponding mass loading.

marked for each mass loading, assuming that the water sprays are fully gasified. In general, propagation of hydrogen/air detonation is considerably influenced by both water droplet size and mass loading. Figure 3 can be divided into two regimes. Specifically, the cases left to the dashed line correspond to successful detonation propagation in the two-phase section. For these cases, the lower the water mass loading, the stronger the detonative combustion. This is featured by the lower velocity deficits relative to the C–J speed from the droplet-free H_2 /air mixture. Some of them are selected to be further simulated with extended length (i.e., $x = 0.22\text{--}0.4 \text{ m}$) of the two-phase section, and it is shown that the DW can still propagate beyond $x = 0.3 \text{ m}$.

Moreover, the rest cases with open symbols correspond to detonation extinction, characterized by the ultimate decoupling of the reaction and leading shock fronts after the DW's travel a finite distance in the two-phase section. When the mass loading z is beyond 0.6 (correspondingly $\rho > 0.252 \text{ kg/m}^3$), detonation extinction always occurs, regardless of the droplet diameters (i.e., $2.5\text{--}15 \mu\text{m}$). However, when $z < 0.6$, the droplet diameter effects appear. Specifically, for a fixed mass loading, the DWs are quenched with relatively small d_d^0 , and the critical diameter for detonation extinction decreases with smaller z . The pure gas cases ($d_d^0 = 0$ in Fig. 3) are also run when the liquid water is fully vaporized (with $T_0 = 300 \text{ K}$ and $p_0 = 50 \text{ kPa}$). One can see that, except with $z = 0.031$, the detonations are quenched for all the loadings, because water vapor has stronger kinetic weakening effect. This indicates that the H_2 /air mixtures with the above diluent concentrations cannot support detonation propagation. This tendency is also seen with ultra-fine droplets (e.g., $2.5 \mu\text{m}$), implying that the significant kinetic contributions of the water vapor from their evaporation. The reason for the effects of water droplets on detonation propagation speed will be discussed in Sec. V C.

Nine representative two-phase cases will be discussed in detail in the following, which are cases a–g in Table I. Specifically, cases a, b2, and c–g are selected to study the water mass loading effects with a fixed droplet diameter, that is, $d_d^0 = 10 \mu\text{m}$. Furthermore, cases b1, b2, and b3 with the same mass loading $z = 0.31$ are used to examine the influence of initial droplet size on propagation and extinction of detonation waves. The cases in Table I are also marked in Fig. 3. Moreover, the purely gaseous detonation in stoichiometric H_2 /air mixture, case h, is also simulated as a reference case.

TABLE I. Selected simulation cases.

Case	Mass loading z	Diameter $d_d^0/\mu\text{m}$	
Two-phase mixture (H_2 /air + water droplets)	a	0.155	10
	b	0.31	5
	2		10
	3		15
	c	0.465	10
	d	0.545	
	e	0.62	
	f	0.775	
	g	0.93	
Purely gaseous mixture (H_2 /air)	h

B. Reaction zone structure of detonation in water mists

Figure 4 shows the instantaneous pressure, temperature, and heat release rate from case b2 ($z = 0.31$ and $d_d^0 = 10 \mu\text{m}$). It is shown that the DW can stably propagate in the two-phase section with multiple transverse waves and detonation heads. Due to droplet evaporation, the gas temperature is reduced to about 1600 K at around $x = 0.224\text{--}0.26 \text{ m}$, different from purely gaseous detonation.^{17,54} Heat release mainly occurs behind the leading shock front (SF) and transverse wave (TW). In addition, compared with droplet-free case (see Sec. D of the Supplementary Document), spray detonations have weaker intensity of leading shock front, featured by generally lower peak pressure around TW and TP, lower temperature behind the SF, and smaller heat release rate behind the incident waves (IW). Figure 5

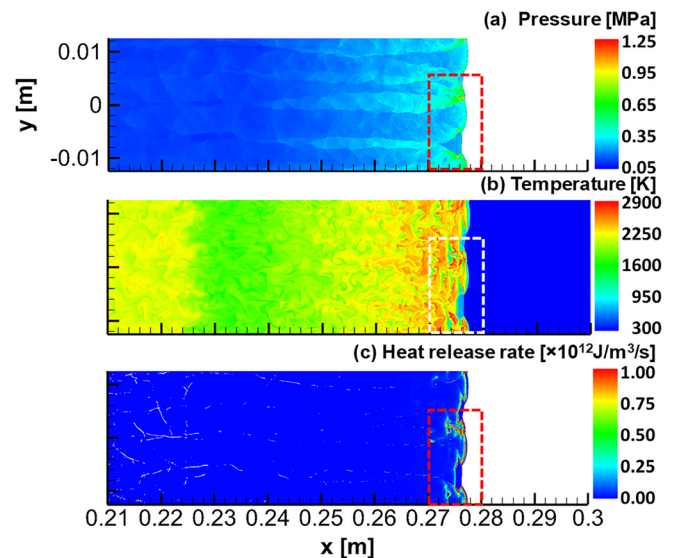


FIG. 4. Distributions of (a) pressure, (b) temperature, and (c) heat release rate in the two-phase section. Results from case b2: $z = 0.31$ and $d_d^0 = 10 \mu\text{m}$.

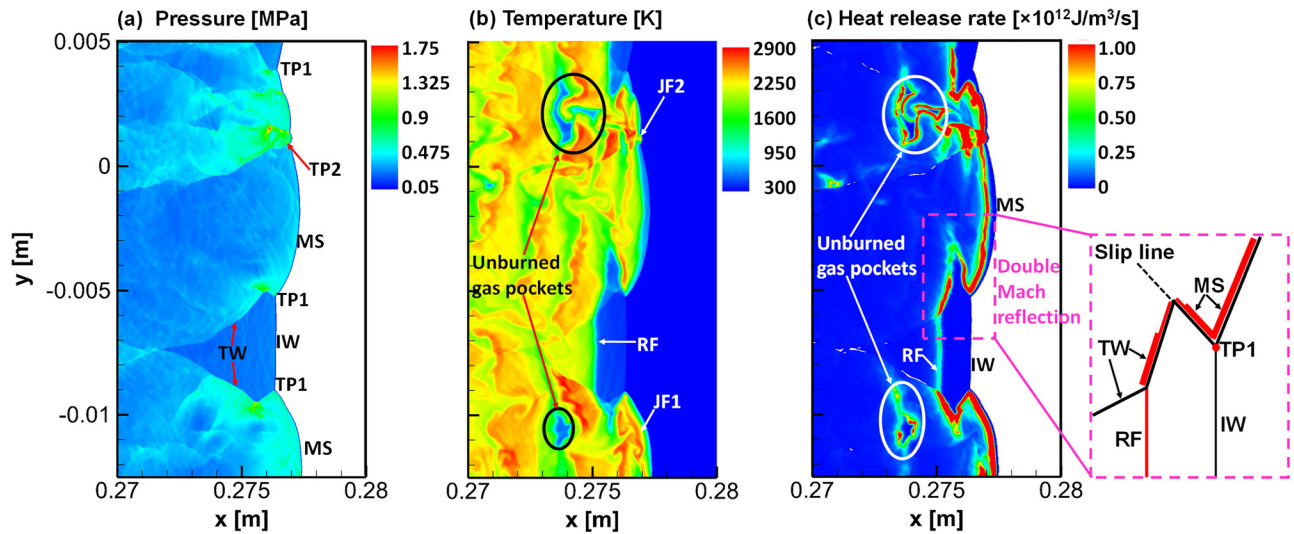


FIG. 5. Close-up view of detonation frontal structure in the dashed box in Fig. 4: (a) pressure, (b) temperature, and (c) heat release rate. Results from case b2: $z = 0.31$ and $d_d^0 = 10 \mu\text{m}$.

shows the enlarged view of the detonation front cellular structure corresponding to the dashed box in Fig. 4. One can see from Fig. 5(a) that the Mach stems (MS), incident waves (IW), TW, and primary/secondary triple points (TP1/TP2) are captured. As marked in Fig. 5(b), the primary and secondary jet flows (JF1 and JF2) are also predicted, which are, respectively, generated through Richtmyer–Meshkov instability (RMI)⁵⁵ and collision between the neighboring triple points. Pockets of the unreacted gas escape from the main detonation front after the collision of two triple points, as marked in Figs. 5(b) and 5(c).

Moreover, the temperature and heat release rate (HRR) behind the MS are much higher than that behind the IW. Decoupling between the reaction front (RF) and IW can be seen, which further produces the double Mach structure,⁵⁶ as indicated in Fig. 5(c) and the inset. The detailed thermochemical states behind the MS and IW will be further interpreted with CEMA in Sec. V B.

Figure 6 shows the distributions of instantaneous diameter d_d , evaporation rate \dot{m}_d and temperature T_d for Lagrangian water droplets, corresponding to the same instant as in Figs. 4 and 5. The details inside the dashed box are shown in Fig. 7. To describe the droplet evaporating zone, two characteristic locations are denoted in Fig. 6, that is, evaporation onset front (EOF) and end of two-phase section (ETS). In our analysis, EOF corresponds to a location where the local droplet evaporation rate is larger than 1×10^{-9} kg/s, while the end of two-phase section (ETS) is the contact surface between the purely gas- and two-phase mixtures.

As shown in Fig. 6(a), the droplet diameter before the DW remain almost unchanged ($10 \mu\text{m}$), due to limited evaporation. There is negligible droplet evaporation between SF and RF for Mach stem and incident wave alike, as shown in Fig. 7(a). This can also be confirmed in Fig. 8, through which one can see that the mass fractions of O_2 and H_2 and local equivalence ratio in the induction zones are almost the same as those in the initial gas. Moreover, near the EOF, the droplet diameter slightly increases by roughly 1% due to the droplet expansion [also shown in Fig. 7(a)]. This is caused by elevated

droplet temperature [Figs. 6(c) and 7(c)], due to slight droplet density reduction [see Eq. (12)]. Since the mass of the individual droplet is almost not changed, the droplet volume (hence diameter) slightly increases.

Although the gas temperature immediately behind the MS is much higher than that behind the IW, nevertheless, the droplet heating takes a finitely long distance behind both shock waves, as demonstrated in Fig. 7(c). In this case, the distance between the DW and

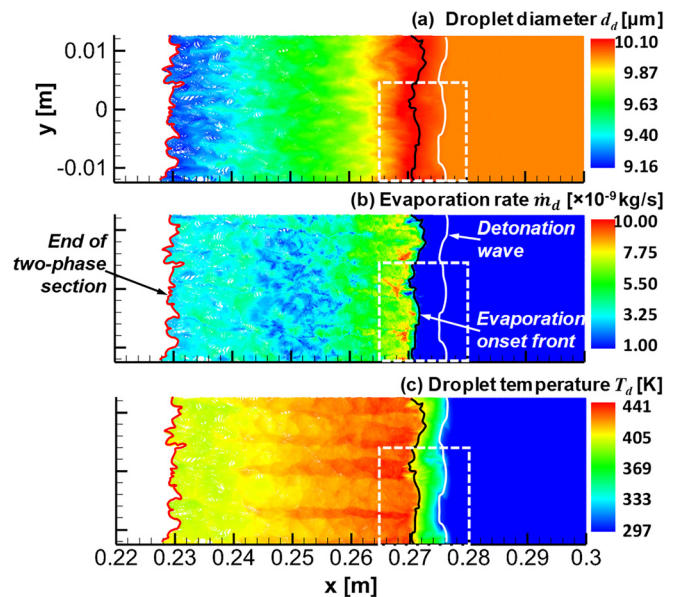


FIG. 6. Distributions of Lagrangian water droplets colored with instantaneous (a) diameter, (b) evaporation rate, and (c) temperature. Results from case b2: $z = 0.31$ and $d_d^0 = 10 \mu\text{m}$.

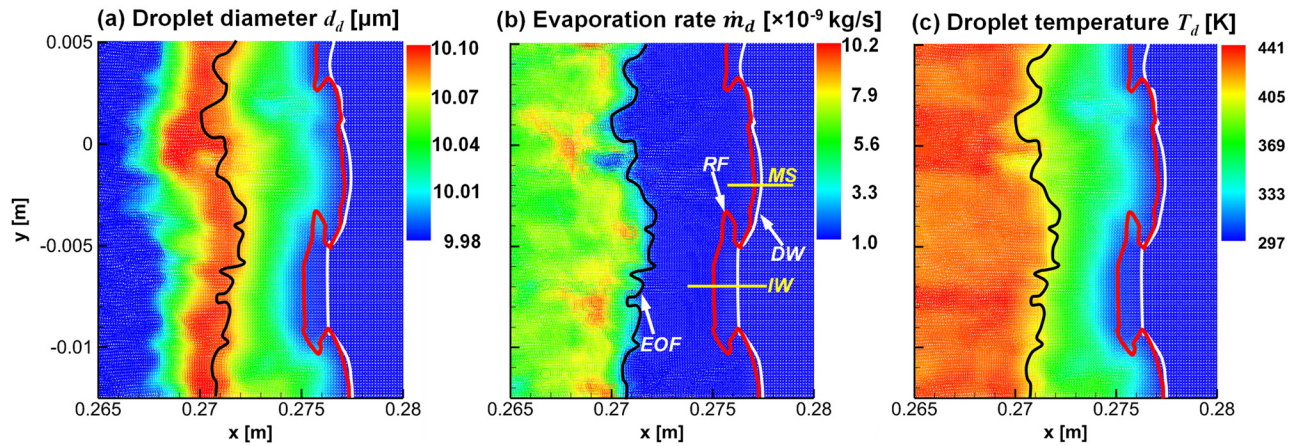


FIG. 7. Close-up view of the Lagrangian droplets in the dashed box in Fig. 6: (a) diameter, (b) evaporation rate, and (c) temperature. Results from case b2: $z = 0.31$ and $d_d^0 = 10 \mu\text{m}$.

EOF is about 5 mm, which is smaller than the counterpart result (about 10 mm) in $\text{C}_2\text{H}_4/\text{air}$ detonation in water sprays.¹⁷ This is reasonable because larger droplet diameter ($15.9 \mu\text{m}$) is considered in Ref. 17, and hence, longer droplet heating period is expected. The droplet temperature is increased to 440 K around the EOF and strong droplet evaporation then occurs. Note that the heated droplets mainly exist behind the Reaction Front (RF in Fig. 7) where pronounced heat release occurs. The evaporation continues in the post-detonation area [see Fig. 6(b)], although the evaporation rate slightly decreases further downstream. This may be associated with the lower gas and water droplet temperatures, as demonstrated in Figs. 4(b) and 6(c).

C. Droplet mass loading effects

To demonstrate the influences of water spray mass loading on H_2/air detonations, numerical soot foils are demonstrated in Fig. 9, which are recorded from the trajectory of maximum pressure location

when the DW propagates in the two-phase section. It is known that these tracks are closely associated with the triple points on the detonation front and the cell apices are the loci of triple point collision.⁵⁷ Gaseous detonation, case h, is also included in Fig. 9(h) for comparison. It can be observed that the presence of water droplets considerably changes the peak pressure trajectories of stoichiometric H_2/air detonations. Note that the DWs cannot stably propagate if the water sprays are fully gasified in case a–g, as presented in Fig. 3, and the numerical soot foil, for example, from $z = 0.31$ shown in Fig. 9(i). As a gas-only case, Fig. 9(i) with fully gasified water has a water loading of 0.31. The value of $Y_{\text{H}_2\text{O}}$ indicated near that figure is the mass fraction of water vapor (gas phase). In addition, in the upstream of the two-phase section, the cells of cases a–c increase with mass loading, that is, 5.9, 7.3, and 8.9 mm, which are higher than that in case h (5.2 mm). This tendency is also observed in $\text{C}_2\text{H}_4/\text{air}/\text{water}$ sprays experiments by Jarsalé *et al.*¹⁶ In general, the cell width is proportional to the induction length,^{58–60} which may increase due to stronger evaporating cooling and/or momentum exchange as z increases. Moreover, this spatial variation of the cells is not reported by Watanabe *et al.*¹⁷ in their simulations of the $\text{C}_2\text{H}_4/\text{air}$ detonations in water sprays. It may be related to the higher reduced activation energy of hydrogen/air mixture. Furthermore, in cases a–c, the leading shock wave propagation speed within one cell varies from 0.4 and 1.4 of the C–J velocity, and these deviations are close to those in gaseous detonations.^{58,61,62}

Two striking features emerge due to the movement of triple points (indicated by the white arrows in Fig. 9): merged trajectory in Fig. 9(a) and re-amplification of the new triple points in Figs. 9(b) and 9(c). The latter is also observed in the simulations of gaseous detonation propagation in channels with porous walls and is attributed to the interactions of transverse wave with different intensities.⁶³ However, transition into the single head mode is not seen in our results, different from the observations from ethylene/air detonation in water sprays.¹⁶

For the cases d–g, the DW propagates a distance in the two-phase section, and then, the leading shock front and reaction front decouples. This is characterized by the quickly reduced peak pressure and therefore faded trajectories in Figs. 9(d)–9(g). Moreover, when the mass loading increases, the detonation extinction occurs earlier.

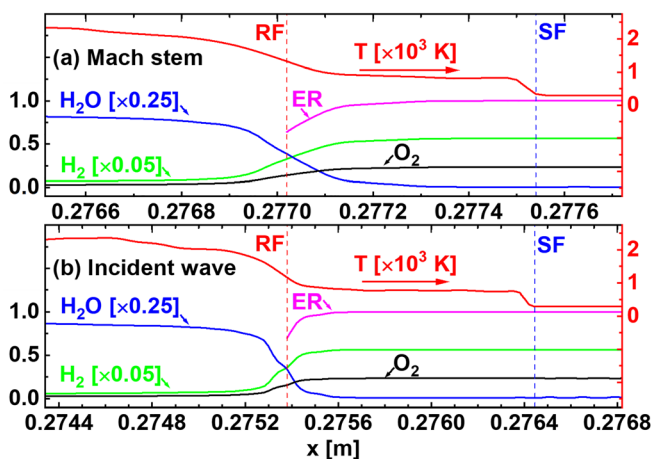


FIG. 8. Spatial distributions of local equivalence ratio and species mass fractions between RF and SF: (a) Mach stem and (b) incident wave. Results extracted from yellow lines in Fig. 7(b).

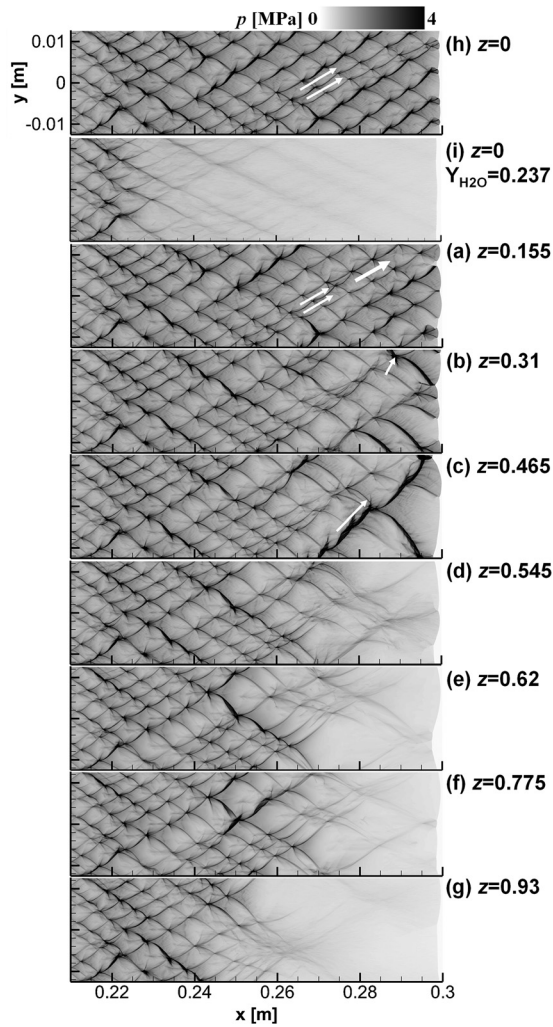


FIG. 9. Numerical smoked foils of (h-i) gaseous and (a-g) two-phase detonations with different mass loadings.

Figure 10 further quantifies the detonation extinction process through the time evolutions of averaged HRR in the corresponding cases in Fig. 9. They are compiled from the two-phase section ($x = 0.2-0.3$ m). The detonation wave enters the two-phase section at about $122 \mu\text{s}$. For cases a and b, the averaged HRR fluctuates regularly and is similar to that of pure gas case h. The periodic variations of heat release rate arise from the collisions between transverse waves and triple points.⁶⁴ However, in case c, when $t > 160 \mu\text{s}$, the HRR gradually increases, which is due to the collisions of the triple points, leading to a new re-amplified one. Their average leading shock speed decreases from 0.92 to $0.83D_{CJ}$, as shown in Fig. 3. For the DW extinction cases (d-g), the heat release gradually decreases. This indicates the global detonation extinction, without any re-initiation.

D. Droplet size effects

Figure 11 shows the numerical soot foils of hydrogen/air detonations with initial water droplet diameters of $5, 10,$ and $15 \mu\text{m}$ (i.e., b1,

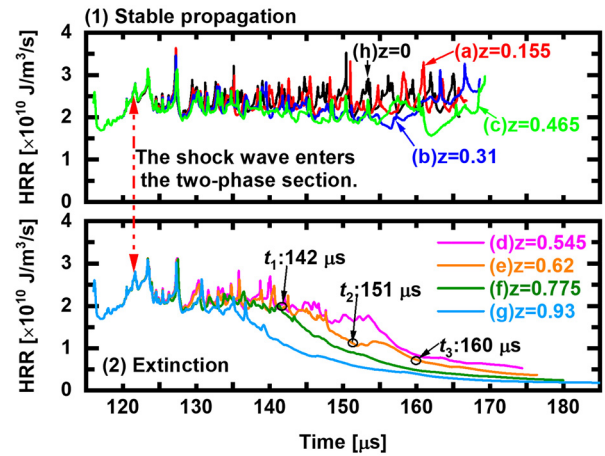


FIG. 10. Temporal evolution of volume-averaged heat release rate in pure gas and two-phase detonations with different mass loadings ($d_d^0 = 10 \mu\text{m}$).

b2 and b3, respectively, in Table I). The water mass loading is fixed to be $z = 0.31$. The reader is reminded that Fig. 11(b) is the same as that in Fig. 9(b). The DW is decoupled after propagating a distance in water sprays with $d_d^0 = 5 \mu\text{m}$. Therefore, the cellular structure in Fig. 11(a) is different from those in Figs. 11(b) and 11(c). For stable detonations, the average cell size in Fig. 11(b) is larger than that in Fig. 11(c) in the second half of the two-phase section. At the same mass loading, smaller droplets indicate large droplet number, and therefore, foregoing influences are more pronounced. Meanwhile, smaller droplets have shorter relaxation time and larger total surface area, either of which may promote the two-phase interaction.

Potted in Fig. 12 are the time evolutions of volume-averaged HRR from three cases in Fig. 11. It is observed that the HRR fluctuates when $d_d^0 = 10$ and $15 \mu\text{m}$. Since triple-point re-amplification is not seen when $d_d^0 = 15 \mu\text{m}$, elevation of HRR at a later stage of DW propagation does not occur at the after $155 \mu\text{s}$. Their averaged shock speeds,

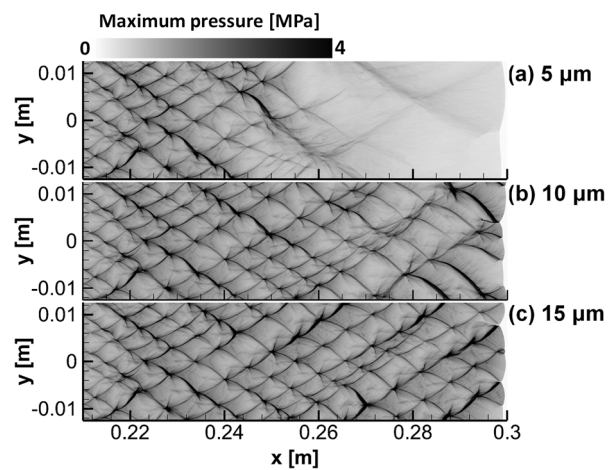


FIG. 11. Numerical smoked foils of two-phase detonations with three droplet diameters: (a) $5 \mu\text{m}$, (b) $10 \mu\text{m}$, and (c) $15 \mu\text{m}$. $z = 0.31$.

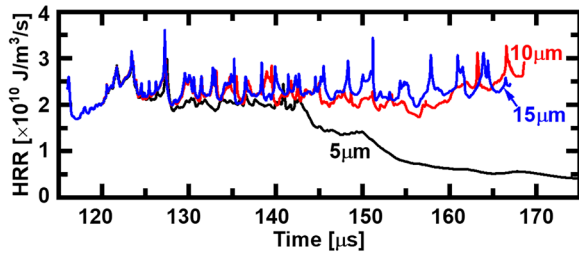


FIG. 12. Temporal evolution of volume-averaged heat release rate with three droplet diameters: (a) $5\ \mu\text{m}$, (b) $10\ \mu\text{m}$, and (c) $15\ \mu\text{m}$. $z = 0.31$.

respectively, correspond to about 86.2% and 89% of the C-J speed D_{CJ} in droplet-free mixture. However, when $d_d^0 = 5\ \mu\text{m}$, the DW fails with continuously reduced HRR in Fig. 12.

V. DISCUSSION

A. Detonation extinction transient

It can be seen from Figs. 3, 9, and 11 that when the water mass loading is large or sprayed droplet size is small, hydrogen detonation extinction occurs. In this section, the unsteady detonation extinction process in case e will be further analyzed. Figure 13 shows the time evolutions of gas temperature, water droplet evaporation rate, and water droplet temperature during the detonation extinction process. Note that Lagrangian droplets are visualized in Figs. 13(b) and 13(c). The DW stably propagates at $142\ \mu\text{s}$. At $151\ \mu\text{s}$, partial extinction behind the leading SF can be seen, characterized by the increased distance between the SF and RF at most locations of the leading front. The SF and RF are completely decoupled at $160\ \mu\text{s}$. Meanwhile, one can see from Figs. 13(b) and 13(c) that generally the length of the shocked two-phase section (between SF and ETS) increases when the

DW is gradually weakened. ETS is a critical location demarcating the droplet-laden and droplet-free areas. Due to the spatial delay of the RF relative to the SF, it takes longer for the water droplets to be heated and the evaporation becomes weaker behind the EOF. The two-phase heat exchange further weakens the deflagrative combustion in the shocked hydrogen/air mixtures.

The evolutions of detailed frontal structure in the foregoing extinction process are further illustrated in Fig. 14. It is found that at $149\ \mu\text{s}$ a series of Mach stems (e.g., MS0, MS1, and MS2) exist. As the two triple points of MS1 and MS2 move toward each other, their collision produces the third Mach stem (MS3) at $151\ \mu\text{s}$. However, no chemical reactions proceed at these two triple points, and meanwhile, their pressure superposition does not induce chemical reactions behind MS3. A jet flow, JF1, is generated behind MS3 at $152.5\ \mu\text{s}$. However, this cold jet does not initiate a detonation. When $t = 149\text{--}152.5\ \mu\text{s}$, MS0 is still followed by considerable heat release. At $154\ \mu\text{s}$, however, decoupling of reaction front and lower part of leading shock begins. A new Mach stem, MS4, is produced by the interaction of MS3 and the lower one. Finally, after $t = 157\ \mu\text{s}$, the RF is fully decoupled from the leading SF. Their distance gradually increases, and no detonation initiation is seen.

The profiles of temperatures, velocities, heat release rate, and mass fractions of main species at $142, 151,$ and $160\ \mu\text{s}$ are depicted in Fig. 15. Note that these quantities are obtained through density-weighted averaging along the y -direction. When the SF and RF are gradually decoupled, the gas temperature decreases. Moreover, the droplet temperature distributions are almost not affected. The average gas velocity grows quickly due to the arrival of the SF and decreases to low values after about $30\text{--}40\ \text{mm}$ after the SF, due to momentum exchange with the droplet phase. Also, the peak value is gradually reduced from 142 to $160\ \mu\text{s}$. The droplet velocity slightly increases and is close to that of the gas velocity at around $x_0\text{--}20\ \text{mm}$. Afterward,

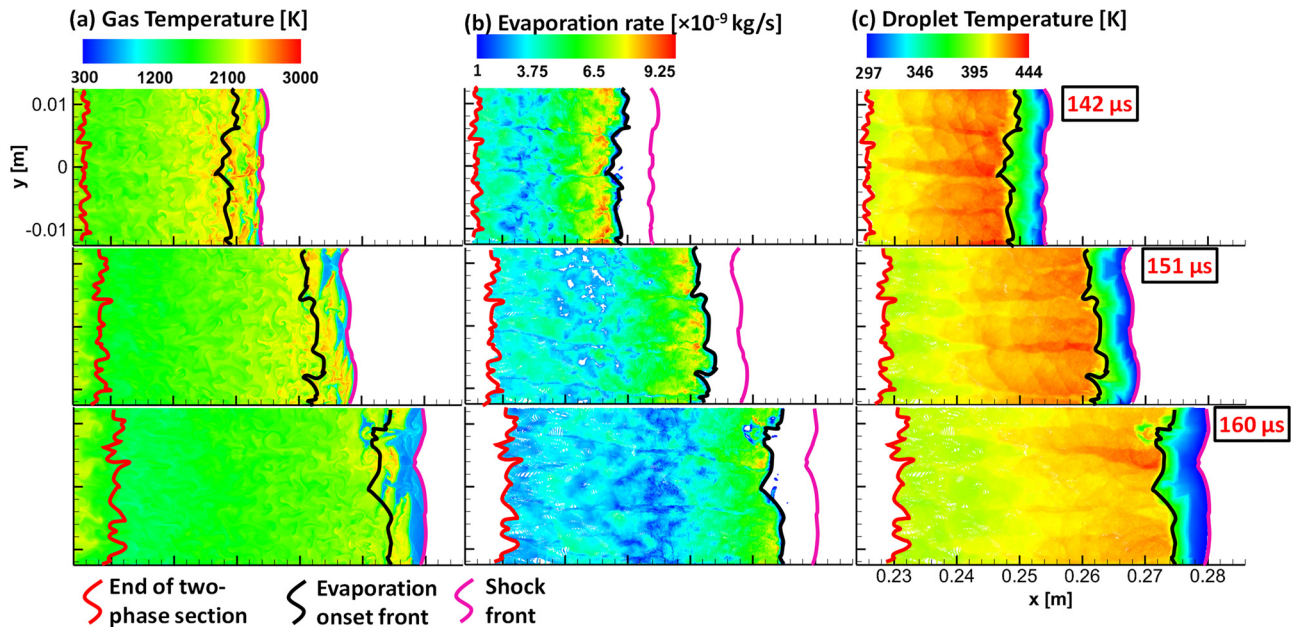


FIG. 13. Evolution of the detonation front in three instants: (a) gas temperature, (b) droplet evaporation rate, and (c) droplet temperature. Results from case e with $z = 0.62$.

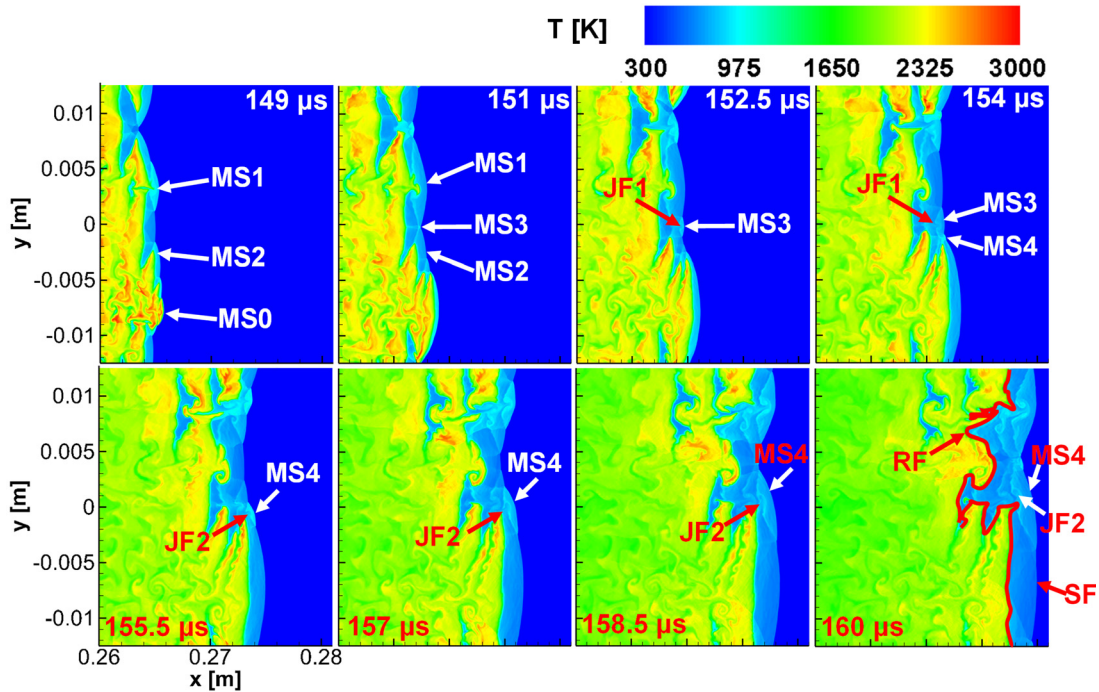


FIG. 14. Evolution of gas temperature during a detonation extinction process.

because of the finite momentum relaxation time, the droplet velocities are even higher than the decaying gas velocities. As such, interphase temperature and velocity equilibria behind the DW are not reached. When the detonation is quenched, the heat release decays quickly, although the length of reaction zone shows limited change (about 10 mm). The H_2O mass fraction increases when the DW propagates forward although it is gradually weakened, due to more evaporating droplets behind the SF. However, HO_2 and H_2O_2 mass fractions decrease because of the weakened gas reactions. The chemical species contributions of the DW will be analyzed in Sec. V B with CEMA.

B. Chemical explosion mode in gaseous detonation

In this section, CEMA^{20,21,65–68} is used to quantify critical gas phase chemical feature in detonations. It has been proven a reliable tool to identify the critical combustion phenomena.^{20,21,69,70} The differential equations for a spatially homogeneous reaction system read

$$\frac{dy}{dt} = \omega(y), \quad (30)$$

where y represents the vector of temperature and species mass fractions. $\omega(y)$ is the chemical source term. In CEMA, eigen-analysis of the local chemical Jacobian is performed:

$$\frac{d\omega}{dt} = \mathbf{J}_\omega \cdot \omega(y), \quad \mathbf{J}_\omega = \frac{\partial \omega}{\partial y}, \quad (31)$$

where \mathbf{J}_ω is the Jacobian matrix of the chemical source term ω . The eigenmode of the Jacobian matrix associated with the eigenvalues of \mathbf{J}_ω , that is, $\lambda_e = \mathbf{b}_e \mathbf{J}_\omega \mathbf{a}_e$, is defined as a chemical explosive mode (CEM) when the real part of λ_e is greater than zero, that is, $\text{Re}(\lambda_e) > 0$.

It should be highlighted that $\text{Re}(\lambda_e)$ corresponds to the reciprocal timescale of the explosion τ_{chem} .²⁰ Here, \mathbf{a}_e and \mathbf{b}_e are, respectively, the right and left eigenvectors associated with the CEM. Note that CEM is a chemical property of local gaseous mixture and indicates the propensity of ignition when the mixture is isolated (constant volume, adiabatic, and droplet-free).²⁰ $\text{Re}(\lambda_e) > 0$ means that the mixture can autoignite, while $\text{Re}(\lambda_e) < 0$ means that it is burnt or fails to autoignite. The condition of $\text{Re}(\lambda_e) = 0$ therefore separates the CEM region and post-combustion or inert mixing one. Moreover, the contributions of temperature or species to the CEM can be evaluated through the explosion index (EI)⁷¹

$$\text{EI} = \frac{|\mathbf{a}_e \otimes \mathbf{b}_e^T|}{\sum |\mathbf{a}_e \otimes \mathbf{b}_e^T|}, \quad (32)$$

where “ \otimes ” denotes element-wise multiplication of two vectors.

Figure 16 shows the spatial evolutions of $\lambda_{CEM} \equiv \text{sign}[\text{Re}(\lambda_e)] \cdot \log_{10}[1 + |\text{Re}(\lambda_e)|]$ at 142, 151, and 160 μs in case e, corresponding to the same instants in Fig. 13. For better illustration, only CEM with positive λ_{CEM} is shown. It is found that CEM exists between the SF and RF. This suggests that the local gaseous mixture is highly explosive. In addition, at 142 μs , the CEM behind the IW and MS is different. For the former, in the induction zone, finite value of λ_{CEM} can only be seen immediately ahead of the RF, corresponding to the short chemical timescale τ_{chem} and hence strong reactivity. However, higher λ_{CEM} (hence low τ_{chem}) exists in the entire induction zone between the RF and MS. In this sense, the mixture behind the MS is intrinsically more explosive than behind the IW. At 151 μs , with increased localized detonation extinctions along the DW, the CEM is more

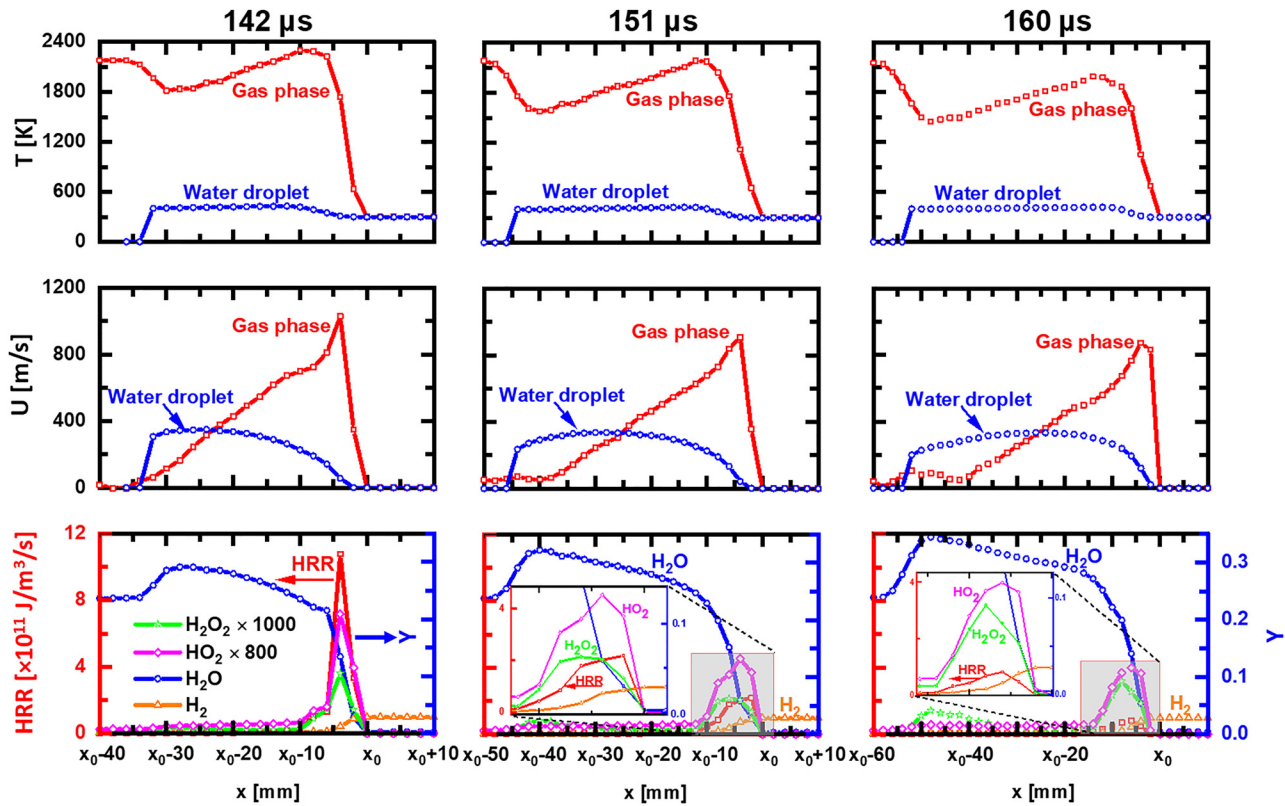


FIG. 15. Spatial distributions of temperature, velocity, heat release rate, and mass fractions of main species at three instants corresponding to Fig. 13. x_0 : the location of reaction front.

distributed as more part of RFs are decoupled from the SF. At 160 μ s, the RF is fully decoupled from the SF, and low values of λ_{CEM} dominate between the RF and SF, although the high λ_{CEM} are still seen near the RF. This implies that the chemical explosion propensity of the shocked gas is further reduced at 160 μ s.

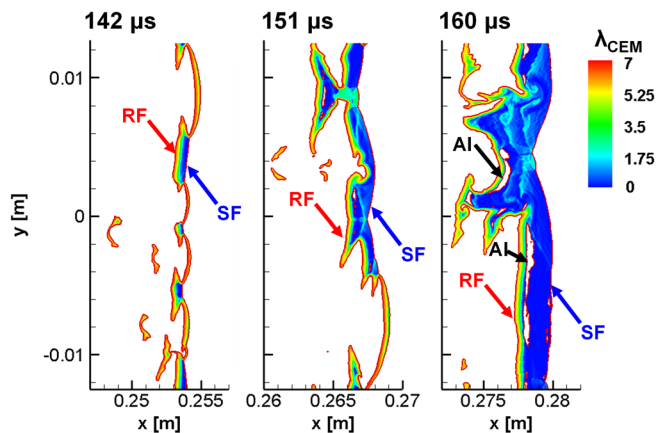


FIG. 16. Distributions of the CEM in a detonation extinction process. Results from case e: $d_0^0 = 10 \mu$ m and $z = 0.62$. Rightmost lines: shock front (SF); the rest iso-lines: reaction front (RF); autoignition: AI.

Figure 17 presents the spatial distributions of EIs for temperature and radicals, which are involved non-trivially in CEM. At 142 μ s, the contributions from temperature are generally important between the RF and SF. Nevertheless, at 151 and 160 μ s, the EIs of radicals, such as HO_2 and H_2O_2 , increase immediately behind the SF. It has been suggested that the local chemical reaction is dominated by chain-branching reactions if the radical EI is high, while it is dominated by thermal runaway if temperature plays a more important role.²⁰ Therefore, at 142 μ s with stable detonations, thermal runaway proceeds behind the SF. Nevertheless, at 151 and 160 μ s, respectively, with partial and global extinctions, most of the mixture in the induction zone is shown to have the propensity to autoignite.

Quantitative comparisons of temperature/species EIs in Fig. 17 are presented in Figs. 18(a)–18(d), which, respectively, correspond to four loci marked by the short lines 1–4 in Fig. 17(a). For each figure, the left (right) end of the x -axis is RF (SF), and therefore, the EI variations inside the induction zone are visualized. Meanwhile, the evolutions of the chemical timescale τ_{chem} in the above-mentioned four locations are demonstrated in Fig. 19. As observed in Fig. 18(a), behind the MS, the CEM is dominant by thermal runaway process in the induction zone and the chemical timescale τ_{chem} is relatively uniform (see Fig. 19). However, behind the IW [Fig. 18(b)], the EIs of the radical species and temperature alternate behind the SF. This is also observed in the chemical propensity within the induction zone of the pulsating n -heptane detonations.⁶⁹ Specifically, at $x > x_{TR1} = 254.08$ mm and

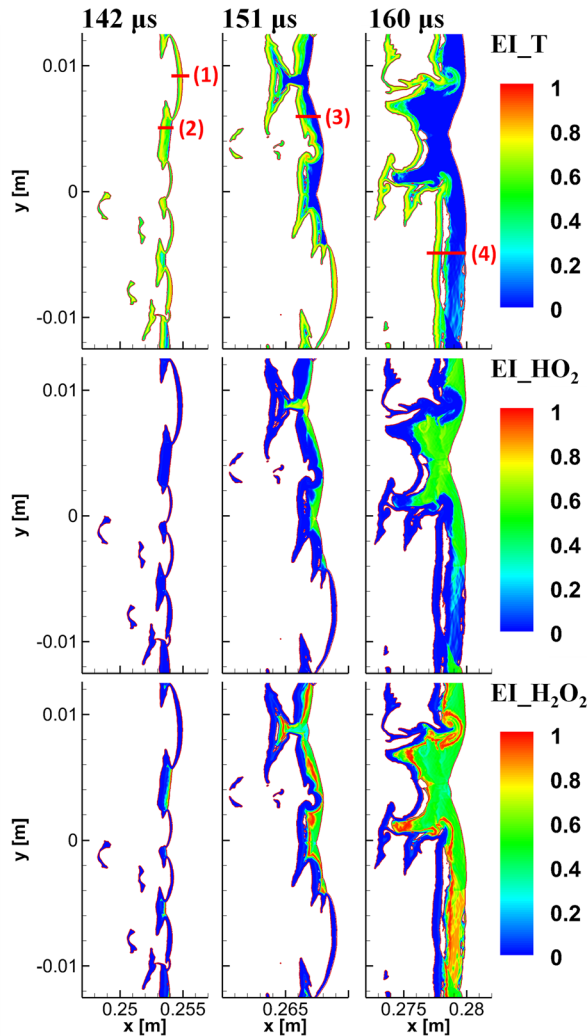


FIG. 17. Distributions of Els of (a) temperature, (b) HO_2 , and (c) H_2O_2 in a detonation extinction process. Results from case $e: d_p^0 = 10 \mu\text{m}$ and $z = 0.62$. Rightmost lines: shock front (SF); the rest isolines: reaction fronts (RF). Lines 1–4: locations of EI profiles in Fig. 18.

$x < x_{TR2} = 253.96 \text{ mm}$, thermal runaway occurs (temperature EI is largest). However, in between, H_2O_2 shows the highest contributions toward the autoignition-dominated CEM. The chemical timescale considerably decreases to $1 \mu\text{s}$ near the RF, as seen in Fig. 19. In Fig. 18(c), the region with thermal runaway CEM is considerably reduced and autoignition CEM is present at $x > x_{TR3} = 266.64 \text{ mm}$. For most of the induction zone ($x > x_{TR3}$), τ_{chem} varies between 0.01 and $10 \mu\text{s}$. In Fig. 18(d) in which complete RF/SF decoupling occurs, the thermal runaway region ($x < x_{TR5} = 278.54 \text{ mm}$) is further reduced.

Interestingly, the region with $\text{Re}(\lambda_c) < 0$ in Figs. 18(d) and 19 is the localized burned island near the RF and surrounded by the mixture with autoignition CEM, as marked with “AI” in Fig. 16. This is caused by the continuously increased induction zone length between the RF and SF in detonation extinction process, which indicates a

longer residence time of the explosive mixture in the shocked area. In addition, radical back diffusion from the RF may also promote the onset of localized AI spots. However, probably due to considerably reduced gas temperature ($< 1200 \text{ K}$, see Fig. 13) in the induction zone, further development of these AI spots into reaction front propagation toward the leading SF is not observed. This is different from the evolutions of local explosions ahead of the traveling RF in one-dimensional *n*-heptane/air detonations, which induces periodic coupling of the SF and RF and hence pulsating detonations.⁶⁹ Beyond $160 \mu\text{s}$, the AI spots are further extended along the spanwise direction before the RF, which may further weaken the RF propagation due to partial reaction of the mixture before the SF.

C. Interaction between detonation and water sprays

To clarify the effects of fine water sprays on hydrogen detonation, interphase exchange of mass, momentum, and energy will be discussed in this section. The density-weighted average interphase transfer rates [S_{mass} , S_{mom} and S_{energy} in Eqs. (26)–(28)] are presented in Fig. 20. A positive mass (energy and momentum) transfer rate indicates that the transfer from liquid (gas) phase to gas (liquid) phase. To explore the water mass loading effects, four cases with stable detonation propagation ($z = 0.031$ – 0.465) are first studied. The results in Fig. 20 correspond to an instant when the DWs lie at the end of the two-phase section ($x_0 = 0.28 \text{ m}$). In general, the transfer rates increase with the water droplet mass loading. Note that although the magnitudes of momentum exchange are rapidly reduced after the SF, kinematic equilibrium is not reached in the detonated gas and at about $x_0 - 20 \text{ mm}$ momentum transfer rate becomes negative, indicating that the momentum transfers from the droplet phase to gas phase. This can be seen clearly in the inset of Fig. 20(c) and is also unveiled from the velocity profiles in Fig. 15. For the role of momentum transfer, drag force is expected to have more direct influence on the detonation wave, while the force associated with droplet evaporation can be negligible (See Fig. S15 of the supplementary material).

It can be observed that energy and momentum exchanges start immediately at x_0 (i.e., SF), but pronounced mass transfer (i.e., droplet evaporation) occurs at $x_0 - 5 \text{ mm}$, well behind both SF and RF. Consequently, the energy and/or momentum transfer (convective heat transfer and/or drag force) are expected to have more direct influence on the RF and SF than the mass transfer (water vapor addition and evaporative cooling). As demonstrated in Fig. 21, when the leading shock propagates in the two-phase area, the shock intensity gradually reduced, mainly due to the weakened coupling between RF and SF. Moreover, at the same location, the leading shock propagation speeds are monotonically reduced when the mass loading z become greater. Furthermore, since there is limited droplet evaporation ahead of RF, chemical reaction in the induction zone is mainly affected by momentum exchange and convective heat transfer between the gas and water sprays. Furthermore, the averaged energy transfer rate further increases when the droplet evaporation becomes strong at around $x_0 - 10 \text{ mm}$, due to the absorption of the latent heat. For the role of energy transfer [see Eq. (28)], convective heat transfer is much more important than water vapor enthalpy. Therefore, although mass transfer occurs after the RF, however, it can still indirectly weaken the gas temperature around the RF through heat conduction. This can also be observed in Figs. 15.

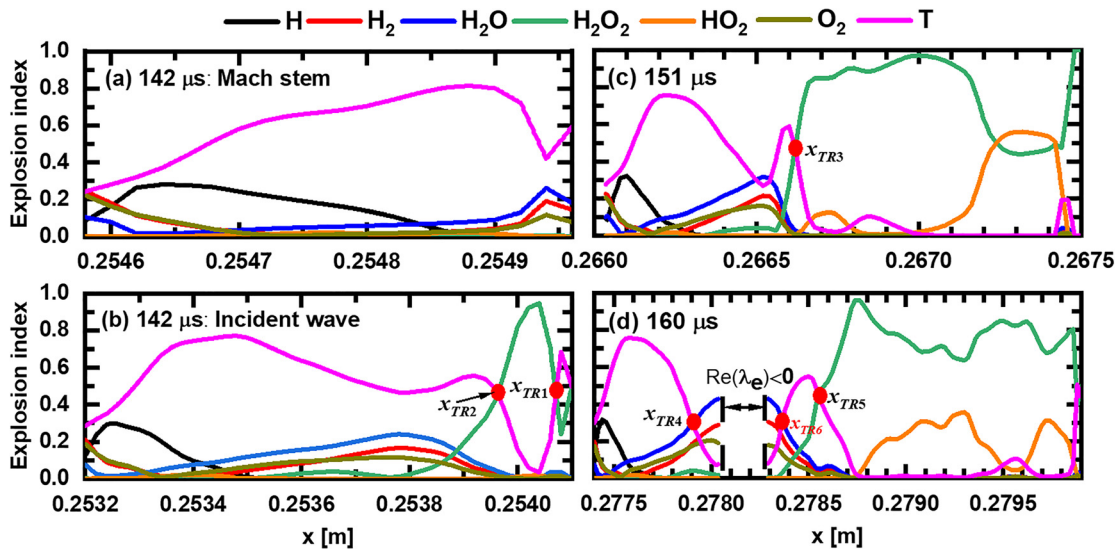


FIG. 18. Spatial distributions of EIs: (a) and (b) 142 μ s, (c) 151 μ s, and (d) 160 μ s in a detonation 617 extinction process along the lines 1–4 in Fig. 17(a). Red dots: transition loci for thermal runaway 618 and radical explosion.

The interphase transfer rates in stable detonations subject to different droplet mass loadings and droplet diameters are demonstrated in Fig. 22, which correspond to one instant of stable DWs in Fig. 3. They are averaged between the SF and shock-frame sonic plane (SP),⁷² and the same strategy is also implemented for Figs. 23 and 26. One can see from Fig. 22 that for the same droplet size (e.g., 10 μ m), the rates of mass, energy, and momentum increase with the water mass loading. Moreover, under the same mass loading (e.g., 0.1), the smaller the droplet size, the larger the interphase exchange rates. However, initial droplet size has less influence on the momentum transfer rate when the mass loading is varied from 0.031 to 0.155. When it increases from 0.31 to 0.465, larger difference of the momentum transfer rates is clearly observed.

The evolutions of averaged interphase transfer rates and HRR in detonation extinction process (case e) are shown in Fig. 23. For comparison, the counterpart results from a stable detonation case (case b2) are also presented. Note that HRR is calculated based on the two-phase section. One can see from Fig. 23(a) that the momentum and energy transfer rates instantly increase when the DW enters the

two-phase section. This is because more water droplets are involved as the DW travels forward. Thereafter, interphase transfer rates and HRR in Fig. 23(a) are reduced with the propagation time due to the RF/SF decoupling. The evaporation rate in the extinction case (a) peaks at 0.153 ms because SP is generally extended further downstream.

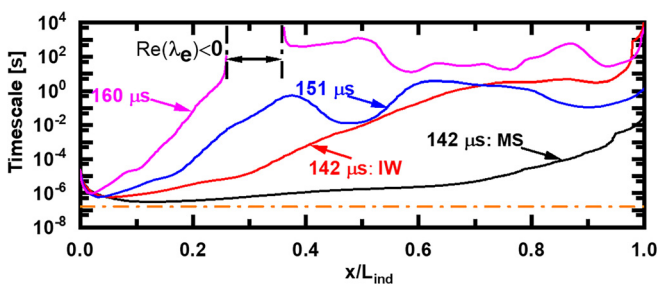


FIG. 19. Spatial distributions of chemical timescale within the induction zone. Dashed line: timescale estimated from induction zone length divided by Chapman-Jouguet speed. $x = 0$: reaction front; $x = 1.0$: shock front.

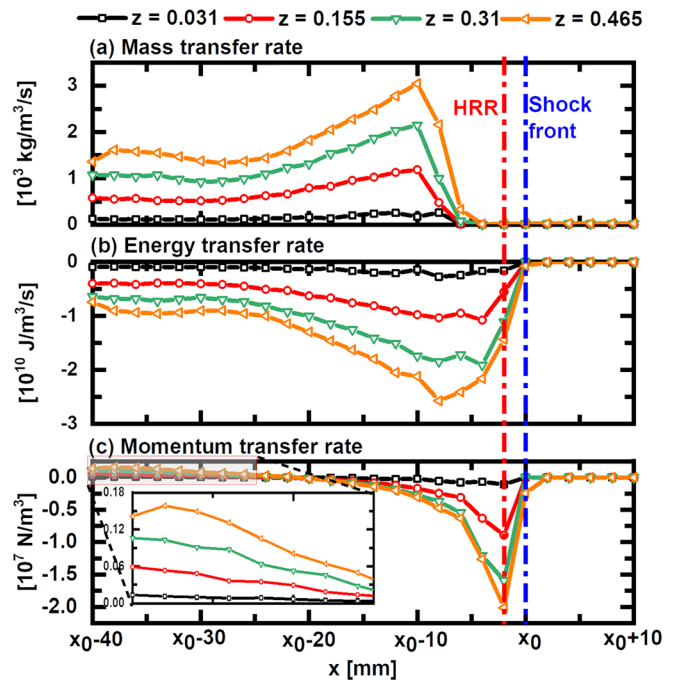


FIG. 20. Profiles of averaged transfer rates of (a) mass, (b) energy, and (c) momentum with various mass loadings. $d_d^0 = 10 \mu$ m. x_0 : leading shock front. RF: reaction front.

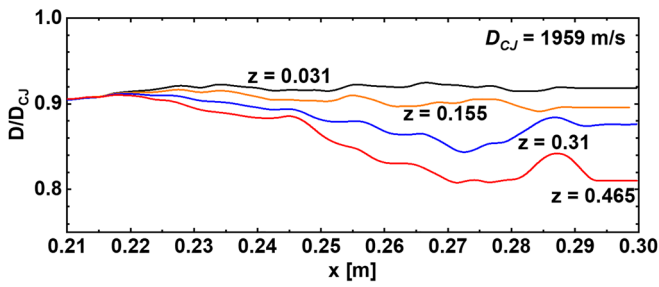


FIG. 21. Non-dimensional propagation velocity with various mass loadings. $d_d^0 = 10 \mu\text{m}$.

These are different from the results of the stable detonation in Fig. 23(b) in which the relatively constant, albeit fluctuating, HRR and momentum and energy transfer rates are observable. However, obvious delay (about $5 \mu\text{s}$) of mass transfer can be found in both cases. The slight reduction of averaged mass transfer (about 0.16 ms) is caused by fewer evaporating droplets in the reduced distance between sonic plane and leading shock wave.

Figure 24 further shows the coupling between the DWs and local water sprays in cases e and b2. They are averaged from the domain with full width and 5 mm thickness centering at the RF, thereby covering the RF-SF complex. For both cases, the mass transfer rate is almost zero because the droplet temperatures are still low and this domain lies before the EOF. The energy and momentum transfer rates are almost constant when the detonation is stable, indicating the overall balance between the RF-SF complex and water droplets. However, monotonic decrease in the two rates starts at around $123 \mu\text{s}$, much earlier than those from the counterpart results when the entire domain is considered.

To further clarify the effects of water droplets on detonation extinction, numerical experiments are performed through switching off the respective models for the two-phase interactions. They are

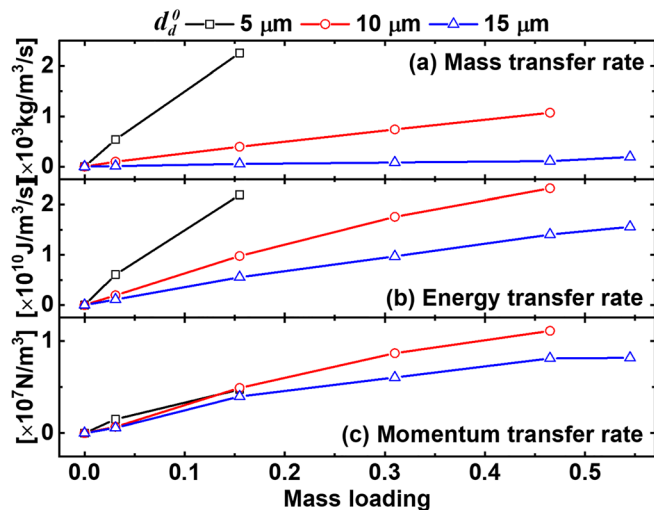


FIG. 22. Averaged interphase transfer rates of (a) mass, (b) energy, and (c) momentum as functions of droplet mass loading and diameter.

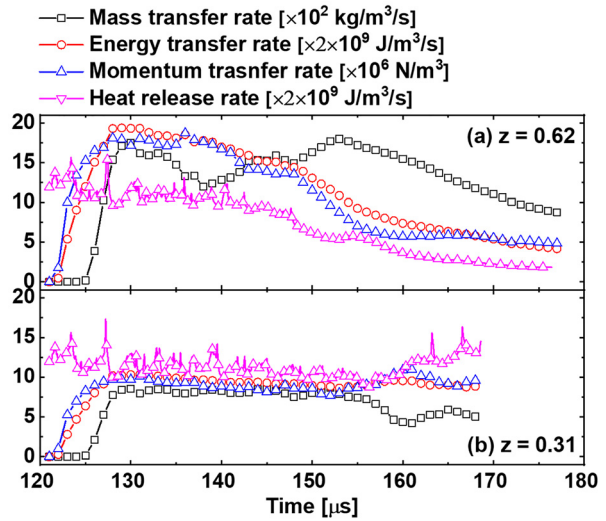


FIG. 23. Time history of averaged interphase transfer rates and combustion HRR with mass loading of (a) 0.62 and (b) 0.31. $d_d^0 = 10 \mu\text{m}$.

based on case e. As tabulated in Table II, e1 considers interphase momentum and energy exchanges (excluding droplet evaporation and latent heat absorption), while e2 only includes momentum exchange. The case e2 aims to isolate the kinematic effects of drag force only. The time histories of averaged HRR based on the whole two-phase section from these cases are illustrated in Fig. 25. It is observed that interphase coupling appreciably affects the DW propagation and their influences become pronounced at $135 \mu\text{s}$ (about $13 \mu\text{s}$ after the DW is transmitted in the water sprays).

As discussed in Sec. V A, the DW in case e is fully extinguished. When the evaporation model is disabled in e1, global extinction is not

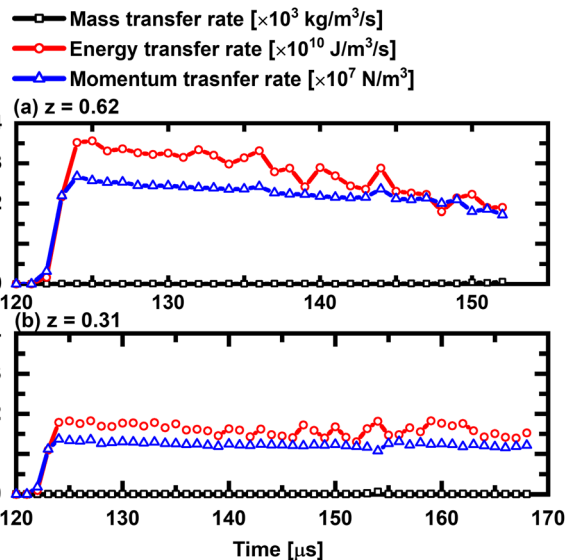


FIG. 24. Time history of volume-averaged interphase transfer rates near the reaction front with mass loading of (a) 0.62 and (b) 0.31. $d_d^0 = 10 \mu\text{m}$.

TABLE II. Numerical experiments for interactions between detonation wave and water droplets.

Case	Drag force	Convective heat transfer	Droplet evaporation and latent heat absorption
e	✓	✓	✓
e1	✓	✓	✗
e2	✓	✗	✗

seen. Conversely, the DW gradually experiences severe localized decoupling between SF and RF and the intensity of the SF is reduced (see Figs. S17 and S18 in the [supplementary material](#)). However, at about 145 μs , a localized ignition spot occurs behind the leading SF, which subsequently evolves into a detonation wave. This corresponds to increased HRR after 150 μs and makes it deviate from the HRR history of case e, as seen from Fig. 25. It is well known that detonation initiation is a stochastic phenomenon, and small perturbation in the gaseous mixture may favorably induce detonation initiation and development.⁷³ In spray detonations, modulation of the local thermochemical states by dispersed droplets may lead to the stochasticity of hot spot. Moreover, in case e2 only with momentum exchange, similar localized DW extinctions are observable (Fig. S18 in the [supplementary material](#)). However, no hot spots are formed, and hence, the averaged HRR in Fig. 25 continuously decreases.

Figure 26 further shows the momentum and energy transfer rates in the three cases. The momentum transfer rate between gas and (non-evaporating/non-heated) droplets in e2 is lower than those in e1 after 160 μs . This is because the averaged post-shock pressures are lower in cases e2. This can be confirmed in Fig. S16 of [supplementary material](#). This corresponds to smaller gas velocities behind SF in case e2 and hence lower interphase momentum exchange. Both momentum and energy exchange in e1 increase after 155 μs due to the detonation development from a hot spot, as discussed in Fig. 25. Overall, the roles of the interphase coupling of energy and mass in hydrogen detonation inhibition can be further confirmed through the foregoing numerical experiments. This is different from the observations in Refs. 12 and 13 in which the momentum extraction from the gas phase is highlighted. This may be because relatively large water droplets are considered in their work, as indicated in Fig. 1. However, the reader should be reminded that the mass, momentum, and energy effects in two-phase reacting flows can be affected by each other, and they are not isolated. For instance, in case e1 and e2, although their ostensible difference is that e2 does not consider heat transfer, however, their

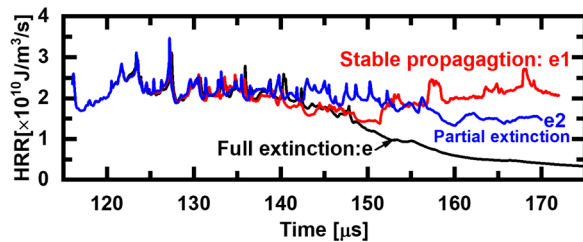


FIG. 25. Time history of volume-averaged heat release rate: effects of mass, momentum, and energy transfer ($z = 0.62$ and $d_d^0 = 10 \mu\text{m}$).

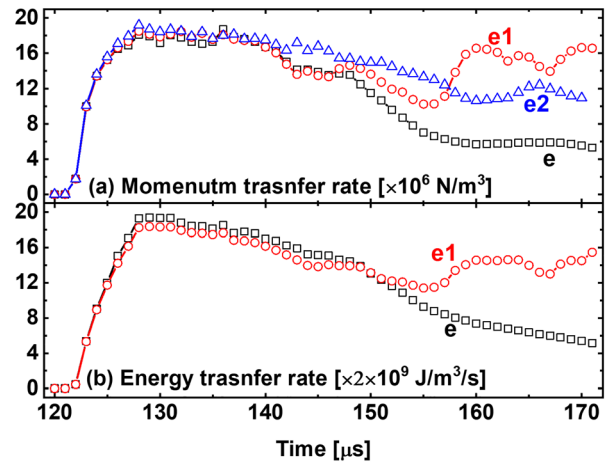


FIG. 26. Transfer rates of (a) momentum and (b) energy between SF and shock-frame SP. ($z = 0.62$ and $d_d^0 = 10 \mu\text{m}$).

momentum transfer is not the same as well, as clearly shown in Fig. 26. Therefore, we would acknowledge that, from these tests, only indicative conclusions can be made.

VI. CONCLUSIONS

Extinction of two-dimensional hydrogen/air detonations in fine water sprays is computationally studied with a hybrid Eulerian-Lagrangian method considering two-way gas-liquid coupling. A detonation extinction map parameterized by water droplet size and mass loading is predicted and shows whether the gaseous detonation can stably propagate in water mists depends on the water mass loading and initial droplet size.

General features of gas phase and liquid droplets, and detailed detonation structures are well captured. The influence of water droplet mass loading on the hydrogen detonation is examined by the trajectories of peak pressure, and the numerical results indicate that the increased mass loading leads to detonation extinction. Meanwhile, the larger the mass loading, the earlier the extinction occurs in the two-phase section. Furthermore, smaller water droplet size would also lead to extinction of the detonation waves.

Detonation extinction analysis is performed with the evolutions of detonation frontal structure, the spatial distribution of thermochemical variables, and interphase transfer rates. It is shown that the droplets need longer time to be heated, and the evaporation becomes weaker behind the EOF due to the spatial delay of the RF relative to the SF. No chemical reactions proceed at these triple points, and meanwhile, their pressure superposition does not induce chemical reactions behind MS. The distributions of temperature and velocity indicate that interphase temperature and velocity equilibria behind the DW are not reached due to the spatially varying gas properties and droplet relaxation time behind the leading shock. In detonation extinction process, heat release and $\text{HO}_2/\text{H}_2\text{O}_2$ mass fractions are reduced, while H_2O mass fraction increases. Moreover, the detailed information of the chemical reaction in the detonation extinction process is analyzed with the chemical explosive mode analysis. The analysis confirms that the shocked gas in the induction zone is highly explosive.

For stable detonations, thermal runaway dominates CEM behind the Mach stem, whereas for those behind the incident wave, autoignition and temperature play alternately dominant roles. When the induction zone increases as the reaction front and shock front are decoupled, localized burned pockets surrounded by the autoignition CEM can be observed.

In addition, the interactions between the detonation wave and water droplets are discussed. The energy and momentum transfer would have stronger influence on the shock front and reaction front than the mass transfer, which starts well behind the detonation wave. It is also found that the interphase exchange rates increase with the water mass loading. Under the same mass loading, the smaller the droplet size, the larger the interphase transfer rates. Moreover, high energy and mass transfer rates are observed at the onset of detonation extinction, and they gradually decrease when the reaction and detonation fronts are decoupled.

In this work, only stoichiometric hydrogen/air mixture is considered. However, for fuel-lean or fuel-rich mixtures, detonation cell size increases considerably,⁷⁴ which demonstrates stronger detonation instabilities. How they respond to fine water droplets merits further study.

SUPPLEMENTARY MATERIAL

See the [supplementary material](#) for the sensitivity analysis about mesh resolution, droplet resolution, and sub-models for two-phase flow modeling.

ACKNOWLEDGMENTS

This work used the computational resources of ASPIRE 1 Cluster in The National Supercomputing Centre, Singapore (<https://www.nsc.sg>). Yong Xu is supported by the NUS Research Scholarship. Professor Zhuyin Ren and Dr. Wantong Wu at Tsinghua University are thanked for sharing the CEMA subroutines.

AUTHOR DECLARATIONS

Conflict of Interest

The authors have no conflicts to disclose.

DATA AVAILABILITY

The data that support the findings of this study are available from the corresponding author upon reasonable request.

REFERENCES

- E. S. Oran, G. Chamberlain, and A. Pekalski, "Mechanisms and occurrence of detonations in vapor cloud explosions," *Prog. Energy Combust. Sci.* **77**, 100804 (2020).
- G. Atkinson, E. Cowpe, J. Halliday, and D. Painter, "A review of very large vapour cloud explosions: Cloud formation and explosion severity," *J. Loss Prev. Process Ind.* **48**, 367–375 (2017).
- C. Catlin, "Passive explosion suppression by blast-induced atomisation from water containers," *J. Hazard. Mater.* **94**, 103–132 (2002).
- G. O. Thomas, "On the conditions required for explosion mitigation by water sprays," *Process Saf. Environ. Prot.* **78**, 339–354 (2000).
- G. Grant, J. Brenton, and D. Drysdale, "Fire suppression by water sprays," *Prog. Energy Combust. Sci.* **26**, 79–130 (2000).
- R. Zheng, K. Bray, and B. Rogg, "Effect of sprays of water and NaCl-water solution on the extinction of laminar premixed methane-air counterflow flames," *Combust. Sci. Technol.* **126**, 389–401 (1997).
- Y. Song and Q. Zhang, "Quantitative research on gas explosion inhibition by water mist," *J. Hazard. Mater.* **363**, 16–25 (2019).
- L. R. Boeck, A. Kink, D. Oezdin, J. Hasslberger, and T. Sattelmayer, "Influence of water mist on flame acceleration, DDT and detonation in H₂-air mixtures," *Int. J. Hydrogen Energy* **40**, 6995–7004 (2015).
- G. Jourdan *et al.*, "Attenuation of a shock wave passing through a cloud of water droplets," *Shock Waves* **20**, 285–296 (2010).
- A. Chauvin, G. Jourdan, E. Daniel, L. Houas, and R. Tosello, "Experimental investigation of the propagation of a planar shock wave through a two-phase gas-liquid medium," *Phys. Fluids* **23**, 113301 (2011).
- K. C. Adiga, H. D. Willauer, R. Ananth, and F. W. Williams, "Implications of droplet breakup and formation of ultra fine mist in blast mitigation," *Fire Saf. J.* **44**, 363–369 (2009).
- R. Ananth, H. D. Willauer, J. P. Farley, and F. W. Williams, "Effects of fine water mist on a confined blast," *Fire Technol.* **48**, 641–675 (2012).
- D. A. Schwer and K. Kailasanath, "Numerical simulations of the mitigation of unconfined explosions using water-mist," *Proc. Combust. Inst.* **31**, 2361–2369 (2007).
- G. O. Thomas, M. J. Edwards, and D. H. Edwards, "Studies of detonation quenching by water sprays," *Combust. Sci. Technol.* **71**, 233–245 (1990).
- U. Niedzielska, L. J. Kapusta, B. Savard, and A. Teodorczyk, "Influence of water droplets on propagating detonations," *J. Loss Prev. Process Ind.* **50**, 229–236 (2017).
- G. Jarsalé, F. Virot, and A. Chinnayya, "Ethylene-air detonation in water spray," *Shock Waves* **26**, 561–572 (2016).
- H. Watanabe, A. Matsuo, K. Matsuoka, A. Kawasaki, and J. Kasahara, "Numerical investigation on propagation behavior of gaseous detonation in water spray," *Proc. Combust. Inst.* **37**, 3617–3626 (2019).
- H. Watanabe, A. Matsuo, A. Chinnayya, K. Matsuoka, A. Kawasaki, and J. Kasahara, "Numerical analysis of the mean structure of gaseous detonation with dilute water spray," *J. Fluid Mech.* **887**, A4-1–40 (2020).
- H. Watanabe, A. Matsuo, A. Chinnayya, K. Matsuoka, A. Kawasaki, and J. Kasahara, "Numerical analysis on behavior of dilute water droplets in detonation," *Proc. Combust. Inst.* **38**, 3709 (2020).
- T. F. Lu, C. S. Yoo, J. H. Chen, and C. K. Law, "Three-dimensional direct numerical simulation of a turbulent lifted hydrogen jet flame in heated coflow: A chemical explosive mode analysis," *J. Fluid Mech.* **652**, 45–64 (2010).
- W. Wu, Y. Piao, Q. Xie, and Z. Ren, "Flame diagnostics with a conservative representation of chemical explosive mode analysis," *AIAA J.* **57**, 1355–1363 (2019).
- W. Sutherland, "LII. The viscosity of gases and molecular force," *London, Edinburgh, Dublin Philos. Mag. J. Sci.* **36**, 507–531 (1893).
- B. E. Poling, J. M. Prausnitz, and J. P. O'Connell, *The Properties of Gases and Liquids* (McGraw-Hill, New York, 2001), Vol. 5.
- B. McBride, S. Gordon, and M. Reno, *Coefficients for Calculating Thermodynamic and Transport Properties of Individual Species* (National Aeronautics and Space Administration, 1993), p. 4513.
- G. B. Macpherson, N. Nordin, and H. G. Weller, "Particle tracking in unstructured, arbitrary polyhedral meshes for use in CFD and molecular dynamics," *Commun. Numer. Methods Eng.* **25**, 263–273 (2009).
- C. T. Crowe, J. D. Schwarzkopf, M. Sommerfeld, and Y. Tsuji, *Multiphase Flows with Droplets and Particles*. (CRC Press, New York, 1998).
- R. H. Perry, D. W. Green, and J. O. Maloney, *Perry's Chemical Engineers' Handbook*, 7th ed. (McGraw-Hill, 1998), p. 35.
- N. A. Fuchs, *Evaporation and Droplet Growth in Gaseous Media*, edited by R. S. Bradley (Pergamon Press, 1959).
- S. S. Sazhin, "Advanced models of fuel droplet heating and evaporation," *Prog. Energy Combust. Sci.* **32**, 162–214 (2006).
- Z. Huang, M. Zhao, and H. Zhang, "Modelling n-heptane dilute spray flames in a model supersonic combustor fueled by hydrogen," *Fuel* **264**, 116809 (2020).
- W. E. Ranz and W. R. Marshall, "Evaporation from drops, Part I," *Chem. Eng. Prog.* **48**, 141–146 (1952).
- E. N. Fuller, P. D. Schettler, and J. C. Giddings, "A new method for prediction of binary gas-phase diffusion coefficients," *Ind. Eng. Chem.* **58**, 18–27 (1966).
- E. L. Cussler, *Diffusion: Mass Transfer in Fluid Systems*, 3rd ed. (Cambridge University Press, 2009).

- ³⁴A. B. Liu, D. Mather, and R. D. Reitz, "Modeling the effects of drop drag and breakup on fuel sprays," in SAE Technical Paper (1993).
- ³⁵S. Cheatham and K. Kailasanath, "Numerical modelling of liquid-fuelled detonations in tubes," *Combust. Theory Model.* **9**, 23–48 (2005).
- ³⁶C. B. Henderson, "Drag coefficients of spheres in continuum and rarefied flows," *AIAA J.* **14**, 707–708 (1976).
- ³⁷O. Igra and K. Takayama, "Shock tube study of the drag coefficient of a sphere in a non-stationary flow," *Proc. R. Soc. A* **442**, 231–247 (1993).
- ³⁸G. Tedeschi, H. Gouin, and M. Elena, "Motion of tracer particles in supersonic flows," *Exp. Fluids* **26**, 288–296 (1999).
- ³⁹Z. Huang, M. Zhao, Y. Xu, G. Li, and H. Zhang, "Eulerian–Lagrangian modelling of detonative combustion in two-phase gas-droplet mixtures with OpenFOAM: Validations and verifications," *Fuel* **286**, 119402 (2021).
- ⁴⁰H. G. Weller, G. Tabor, H. Jasak, and C. Fureby, "A tensorial approach to computational continuum mechanics using object-oriented techniques," *Comput. Phys.* **12**, 620 (1998).
- ⁴¹C. J. Greenshields, H. G. Weller, L. Gasparini, and J. M. Reese, "Implementation of semi-discrete, non-staggered central schemes in a collocated, polyhedral, finite volume framework, for high-speed viscous flows," *Int. J. Numer. Methods Fluids* **63**, 1–21 (2010).
- ⁴²H. Zhang, M. Zhao, and Z. Huang, "Large eddy simulation of turbulent supersonic hydrogen flames with OpenFOAM," *Fuel* **282**, 118812 (2020).
- ⁴³M. Zhao, J. M. Li, C. J. Teo, B. C. Khoo, and H. Zhang, "Effects of variable total pressures on instability and extinction of rotating detonation combustion," *Flow, Turbul. Combust.* **104**, 261–290 (2020).
- ⁴⁴M. Zhao and H. Zhang, "Origin and chaotic propagation of multiple rotating detonation waves in hydrogen/air mixtures," *Fuel* **275**, 117986 (2020).
- ⁴⁵M. Zhao and H. Zhang, "Rotating detonative combustion in partially pre-vaporized dilute n-heptane sprays: Droplet size and equivalence ratio effects," *Fuel* **304**, 121481 (2021).
- ⁴⁶M. Zhao and H. Zhang, "Large eddy simulation of non-reacting flow and mixing fields in a rotating detonation engine," *Fuel* **280**, 118534 (2020).
- ⁴⁷Q. Meng, M. Zhao, H. Zheng, and H. Zhang, "Eulerian–Lagrangian modelling of rotating detonative combustion in partially pre-vaporized n-heptane sprays with hydrogen addition," *Fuel* **290**, 119808 (2021).
- ⁴⁸A. Kurganov, S. Noelle, and G. Petrova, "Semidiscrete central-upwind schemes for hyperbolic conservation laws and Hamilton–Jacobi equations," *SIAM J. Sci. Comput.* **23**, 707–740 (2001).
- ⁴⁹M. Ó. Conaire, H. J. Curran, J. M. Simmie, W. J. Pitz, and C. K. Westbrook, "A comprehensive modeling study of hydrogen oxidation," *Int. J. Chem. Kinet.* **36**, 603–622 (2004).
- ⁵⁰Y. Mahmoudi and K. Mazaheri, "High resolution numerical simulation of triple point collision and origin of unburned gas pockets in turbulent detonations," *Acta Astronaut.* **115**, 40–51 (2015).
- ⁵¹K. Mazaheri, Y. Mahmoudi, and M. I. Radulescu, "Diffusion and hydrodynamic instabilities in gaseous detonations," *Combust. Flame* **159**, 2138–2154 (2012).
- ⁵²S. Yungster and K. Radhakrishnan, "Pulsating one-dimensional detonations in hydrogen-air mixtures," *Combust. Theory Model.* **8**, 745–770 (2004).
- ⁵³Z. Liu and A. K. Kim, "A Review of water mist fire suppression systems—Fundamental studies," *J. Fire Prot. Eng.* **10**, 32–50 (1999).
- ⁵⁴R. W. Houim and R. T. Fievisohn, "The influence of acoustic impedance on gaseous layered detonations bounded by an inert gas," *Combust. Flame* **179**, 185–198 (2017).
- ⁵⁵Y. Mahmoudi, K. Mazaheri, and S. Parvar, "Hydrodynamic instabilities and transverse waves in propagation mechanism of gaseous detonations," *Acta Astronaut.* **91**, 263–282 (2013).
- ⁵⁶M. H. Lefebvre and E. S. Oran, "Analysis of the shock structures in a regular detonation," *Shock Waves* **4**, 277–283 (1995).
- ⁵⁷S. O. Saunders, "Experimental observations of the transition to detonation in an explosive gas," *Proc. R. Soc. London., Ser. A: Math. Phys. Sci.* **295**, 13–28 (1966).
- ⁵⁸A. I. Gavrikov, A. A. Efimenko, and S. B. Dorofeev, "A model for detonation cell size prediction from chemical kinetics," *Combust. Flame* **120**, 19–33 (2000).
- ⁵⁹R. A. Strehlow, R. E. Maurer, and S. Rajan, "Transverse waves in detonations. I: Spacing in the hydrogen-oxygen system," *AIAA J.* **7**, 323–328 (1969).
- ⁶⁰R. K. Kumar, "Detonation cell widths in hydrogenoxygendiluent mixtures," *Combust. Flame* **80**, 157–169 (1990).
- ⁶¹V. N. Gamezo, D. Desbordes, and E. S. Oran, "Formation and evolution of two-dimensional cellular detonations," *Combust. Flame* **116**, 154–165 (1999).
- ⁶²E. S. Oran, J. W. Weber, E. I. Stefaniw, M. H. Lefebvre, and J. D. Anderson, "A numerical study of a two-dimensional H₂-O₂-Ar detonation using a detailed chemical reaction model," *Combust. Flame* **113**, 147–163 (1998).
- ⁶³K. Mazaheri, Y. Mahmoudi, M. Sabzpooshani, and M. I. Radulescu, "Experimental and numerical investigation of propagation mechanism of gaseous detonations in channels with porous walls," *Combust. Flame* **162**, 2638–2659 (2015).
- ⁶⁴S. Taileb, J. Melguizo-Gavilanes, and A. Chinnayya, "Influence of the chemical modeling on the quenching limits of gaseous detonation waves confined by an inert layer," *Combust. Flame* **218**, 247–259 (2020).
- ⁶⁵S. H. Lam, "Singular perturbation for stiff equations using numerical methods," in *Recent Advances in the Aerospace Sciences, B. C.*, edited by C. Casci (Springer, Boston, MA, 1985), pp. 3–19.
- ⁶⁶S. H. Lam and D. A. Goussis, "The CSP method for simplifying kinetics," *Int. J. Chem. Kinet.* **26**, 461–486 (1994).
- ⁶⁷S. H. Lam, "Using CSP to understand complex chemical kinetics," *Combust. Sci. Technol.* **89**, 375–404 (1993).
- ⁶⁸S. H. Lam, "Reduced chemistry-diffusion coupling," *Combust. Sci. Technol.* **179**, 767–786 (2007).
- ⁶⁹M. Zhao, Z. Ren, and H. Zhang, "Pulsating detonative combustion in n-heptane/air mixtures under off-stoichiometric conditions," *Combust. Flame* **226**, 285–301 (2021).
- ⁷⁰W. Xie, W. Wu, Z. Ren, H. Liu, and M. Ihme, "Effects of evaporation on chemical reactions in counterflow spray flames," *Phys. Fluids* **33**, 065115 (2021).
- ⁷¹Z. Luo, C. S. Yoo, E. S. Richardson, J. H. Chen, C. K. Law, and T. Lu, "Chemical explosive mode analysis for a turbulent lifted ethylene jet flame in highly-heated coflow," *Combust. Flame* **159**, 265–274 (2012).
- ⁷²J. H. S. Lee and M. I. Radulescu, "On the hydrodynamic thickness of cellular detonations," *Combust. Explos. Shock Waves* **41**, 745–765 (2005).
- ⁷³E. S. Oran and V. N. Gamezo, "Origins of the deflagration-to-detonation transition in gas-phase combustion," *Combust. Flame* **148**, 4–47 (2007).
- ⁷⁴G. Ciccarelli, T. Ginsberg, J. Boccio, C. Economos, K. Sato, and M. Kinoshita, "Detonation cell size measurements and predictions in hydrogen-air-steam mixtures at elevated temperatures," *Combust. Flame* **99**, 212–220 (1994).